



# *In situ* etched graphite felt modified with CuFe<sub>2</sub>O<sub>4</sub>/Cu<sub>2</sub>O/Cu catalyst derived from CuFe PBA for the efficient removal of sulfamethoxazole through a heterogeneous electro-Fenton process

Haiqiang Qi<sup>a,b</sup>, Xuelin Shi<sup>a,b</sup>, Zhibin Liu<sup>a,b</sup>, Zihao Yan<sup>a,b</sup>, Zhirong Sun<sup>a,b,\*</sup>

<sup>a</sup> Department of Environmental Engineering, Faculty of Environment and Life, Beijing University of Technology, Beijing 100124, PR China

<sup>b</sup> National Engineering Laboratory for Advanced Municipal Wastewater Treatment and Reuse Technology, Beijing University of Technology, Beijing 100124, PR China

## ARTICLE INFO

### Keywords:

Graphite felt  
Heterogeneous electro-Fenton process  
Density functional theory  
Degradation pathway  
Toxicity

## ABSTRACT

Heterogeneous electro-Fenton (hetero-EF) catalysts exhibit low electrocatalytic performance and poor stability. To improve the performance of a hetero-EF process for pollutant degradation, an efficient and stable electrode consisting of a CuFe<sub>2</sub>O<sub>4</sub>/Cu<sub>2</sub>O/Cu catalyst on etched graphite felt (EGF) was synthesized in this study. The CuFe<sub>2</sub>O<sub>4</sub>/Cu<sub>2</sub>O/Cu@EGF electrode demonstrated good performance under the applied pH range, high stability, good resistance to the effects of other substances in the water environment, and high efficiency toward the degradation of other pollutants. The degradation mechanism was proposed based on experimental results and theoretical calculation. Mass spectrum analysis and theoretical calculations were employed to identify the intermediate products produced during sulfamethoxazole degradation, and the probable degradation pathways were proposed. Finally, the toxicity of intermediates produced during the degradation process was evaluated by toxicological simulation and experiments performed using *Escherichia coli* and *Chlorella*. These results provide a theoretical basis for the efficient removal of antibiotics present in wastewater.

## 1. Introduction

In recent years, with the continuous increase in the production and use of antibiotics, a growing number of antibiotics has entered the water environments, and unfortunately, the existence of antibiotics has also been detected in drinking water [1,2]. Moreover, the continued addition of antibiotics causes pathogenic bacteria to produce antibiotic-resistant genes, making them resistant to drugs and increasing the potential risk to human health and ecological environment [3–6]. Sulfonamides are one of the antibiotics commonly detected in water environments [7]. Owing to the variety and complexity of sulfonamides in production processes, sulfonamide wastewater is produced in large amounts and has a complex composition with a large amount of bacteriostatic organic matter. These characteristics indicate that sulfa wastewater is toxic to microorganisms [8]. Unfortunately, it is difficult to degrade sulfa wastewater by traditional activated sludge processes, and the effluent water quality generally does not meet water quality standards [9]. Therefore, development of a wastewater treatment technology for the efficient and safe degradation of antibiotic compounds in wastewater

without being affected by water quality conditions, is urgently required as part of water management.

As an electrochemical advanced oxidation technology, electro-Fenton (EF) process is a promising technology for the degradation of pollutants. EF processes have been widely used in the field of sewage treatment due to their advantages such as no added oxidant [10–12]. The principle of EF processes involves the generation of H<sub>2</sub>O<sub>2</sub> on the cathode followed by the reaction of the generated H<sub>2</sub>O<sub>2</sub> with the catalyst (homogeneous ferric salts, heterogeneous catalysts in solution, or catalysts supported on cathodes) to generate strongly oxidizing hydroxyl radicals ( $\cdot\text{OH}$ ) [13,14], which can quickly, efficiently, and non-selectively achieve the harmless treatment of pollutants. In homogeneous EF processes, Fe<sup>2+</sup> catalysts react with H<sub>2</sub>O<sub>2</sub> to generate strong oxidizing free radicals [15]. Although these systems are highly efficient for the degradation of pollutants, they also have several disadvantages including the generation of iron sludge-based pollution and difficult catalyst recovery. Therefore, heterogeneous EF (hetero-EF) systems have been developed by replacing the dissolved Fe<sup>2+</sup> catalyst with a heterogeneous catalyst. These systems offer the advantages such as a

\* Corresponding author at: Department of Environmental Engineering, Faculty of Environment and Life, Beijing University of Technology, Beijing 100124, PR China.

E-mail address: [zrsun@bjut.edu.cn](mailto:zrsun@bjut.edu.cn) (Z. Sun).

<https://doi.org/10.1016/j.apcatb.2023.122722>

Received 9 September 2022; Received in revised form 17 March 2023; Accepted 1 April 2023

Available online 3 April 2023

0926-3373/© 2023 Elsevier B.V. All rights reserved.

wider pH range, more convenient catalyst recovery, simple and facile operation, and fast reaction. Therefore, hetero-EF systems successfully solve the problems associated with homogeneous EF technology [16]. According to the different spatial positions of heterogeneous catalysts in these systems, hetero-EF technology is generally divided into the following two categories: traditional hetero-EF technology (a heterogeneous catalyst in solution) [17–19] and *in situ* hetero-EF technology (a heterogeneous catalyst on a cathode) [20–24]. *In situ* hetero-EF systems have attracted significant research attention in the field of water treatment. These systems exhibit more advantages than traditional hetero-EF systems for the following reasons: 1) The active sites on the cathode realize the *in situ* generation and reaction of  $\text{H}_2\text{O}_2$ , which improves the utilization rate of  $\text{H}_2\text{O}_2$ , so as to avoid the influence of subsequent biological treatment and the secondary pollution caused by  $\text{H}_2\text{O}_2$  entering the environment; and 2) The rapid conversion of  $\text{Fe}^{3+}/\text{Fe}^{2+}$  is realized by using the reducibility of the cathode to avoid the consumption and waste of  $\text{H}_2\text{O}_2$ .

The cathode plays a key role in *in situ* hetero-EF systems because it directly determines the performance of the entire system. The performance of the cathode depends on the generation and catalysis of  $\text{H}_2\text{O}_2$ . In the *in situ* hetero-EF system, carbon materials with corrosion resistance and good electrical conductivity are often used for the generation of  $\text{H}_2\text{O}_2$  at the cathode [25–30]. The activation of  $\text{H}_2\text{O}_2$  to  $\cdot\text{OH}$  is the most important process besides the generation of  $\text{H}_2\text{O}_2$ , which mainly depends on the performance of the metal-based electrocatalyst on the electrode material. However, some electrocatalysts on electrode surfaces are large and get agglomerated, exhibit poor stability, and have excessively low electrocatalytic activity. Moreover, the introduction of an electrocatalyst onto the electrode surface requires a binder with a strong binding effect; nonetheless, it can block the reaction sites and ultimately reduces the overall electrocatalytic performance of the *in situ* hetero-EF cathodes [31]. Therefore, the development of electrocatalysts with high catalytic activity and high stability directly grown in *in situ* on the surface of matrix materials without a binder exhibits great potential for the development of *in situ* hetero-EF processes.

Metal-organic frameworks (MOFs) are crystal materials with two-dimensional (2D) or 3D skeleton network structures formed by metal ion or metal cluster coordination centers. Prussian blue analogues (PBAs) are MOF materials formed by the coordination of metal ions and cyanide, and PBAs are mainly applied in the fields of drug delivery and biosensing. Compared with other synthetic materials, PBAs exhibit some special properties with good chemical stability, high porosity, uniform atomic doping, and adjustable functions. At the same time, the preparation of catalysts using PBAs as precursors after heat treatment can form rough and developed pore structure, which can effectively improve the catalytic performance. Moreover, catalysts derived from PBAs show excellent performance in Fenton-like systems. Therefore, PBAs are expected to show good performance in electrochemical oxygen reduction reaction (ORR).

In this study, etched graphite felt (EGF) prepared by *in situ*  $\text{CoO}_x$  etching method [32] was used as the matrix material to improve the  $\text{H}_2\text{O}_2$  production capacity of an *in situ* hetero-EF system. The EGF matrix material with rough surface and porous structure was conducive to the subsequent loading of an electrocatalyst. The precursor CuFe PBA was *in situ* grown on the EGF surface, which was then calcined at a high temperature to prepare a  $\text{CuFe}_2\text{O}_4/\text{Cu}_2\text{O}/\text{Cu}@EGF$  electrode. Notably, this preparation method did not require the introduction of a binder. An *in situ* hetero-EF system with  $\text{CuFe}_2\text{O}_4/\text{Cu}_2\text{O}/\text{Cu}@EGF$  cathode was constructed for the degradation of sulfamethoxazole (SMX) at pH = 6. The degradation performance, electrode stability, and influence of various parameters were systematically studied. The  $\text{CuFe}_2\text{O}_4/\text{Cu}_2\text{O}/\text{Cu}@EGF$  electrode showed high electrocatalytic activity and high stability during the degradation of SMX, which was attributed to the uniform dispersion of nanoparticles and the enhanced charge transfer efficiency. Finally, the possible degradation mechanism, degradation path, and ecotoxicity analysis of SMX in this system were proposed.

## 2. Materials and methods

### 2.1. Chemicals and materials

Raw GF (RGF) was provided by Hunan Jiuhua Carbon High-Tech Co., Ltd., China. Boron-doped diamond, used as the anode in the *in situ* hetero-EF system, was purchased from Shanghai Jingan Biotechnology Co., Ltd. For details about other chemicals, see [Supplementary Information](#).

### 2.2. Preparation of $\text{CuFe}_2\text{O}_4/\text{Cu}_2\text{O}/\text{Cu}@EGF$ electrode

EGF [32] was used as the base material for the supporting electrocatalyst to produce  $\text{H}_2\text{O}_2$  in the *in situ* hetero-EF system. Aqueous solution (20 mL) containing  $\text{Cu}(\text{NO}_3)_2$  (30 mM) and sodium citrate (45 mM) was rapidly added to aqueous solution of  $\text{K}_3[\text{Fe}(\text{CN})_6]$  (20 mL, 20 mM) and the contents were stirred for 2 min. Next, EGF was immersed in this solution, and CuFe PBA was allowed to grow at room temperature for 24 h to obtain the CuFe PBA@EGF electrode. The obtained CuFe PBA@EGF electrode was calcined at 500 °C under  $\text{N}_2$  atmosphere for 2 h to obtain the EGF cathode modified with  $\text{CuFe}_2\text{O}_4/\text{Cu}_2\text{O}/\text{Cu}$  catalyst.

### 2.3. Characterization and method

Detailed information is provided in the [Supplementary Information](#).

## 3. Results and discussion

### 3.1. Characterization

Scanning electron microscopy (SEM) images of different electrode surfaces are shown in [Fig. 1](#). The surface of RGF was smooth ([Fig. 1a](#) and [b](#)); in contrast, the surface of EGF was very rough and contained many pore structures ([Fig. 1c](#) and [d](#)). This porous structure was beneficial for improving the ORR of the electrode. Furthermore, the porous structure provided more attachment sites for the subsequent uniform catalyst loading and improved stability of the catalyst on the EGF surface. SEM images of CuFe PBA after *in situ* growth on the EGF fiber surface ([Fig. 1e](#) and [f](#)) show that CuFe PBA mainly consists of a cubic structure with a relatively smooth surface. The CuFe PBA particles are densely coated on the EGF surface, which is not conducive to allowing  $\text{O}_2$  to enter the surface of EGF for ORR. However, after high-temperature carbonization, the CuFe PBA skeleton shrank inward and collapsed ([Fig. 1g](#) and [h](#)), transforming the original dense structure of CuFe PBA into a loose and coarse porous structure. This led to opening of channels for  $\text{O}_2$  in solution to enter the EGF surface. Therefore, this morphology was beneficial for the diffusion of  $\text{O}_2$  to the EGF fiber surface for generating  $\text{H}_2\text{O}_2$  via ORR. Moreover, the  $\text{H}_2\text{O}_2$  generated on the EGF electrode could be quickly transferred to the catalytic sites on the CuFe PBA derivatives through the porous structure and got catalyzed to generate strong oxidizing free radicals. Energy-dispersive X-ray spectroscopy (EDS) elemental mapping of  $\text{CuFe}_2\text{O}_4/\text{Cu}_2\text{O}/\text{Cu}@EGF$  ([Fig. 1i–n](#)) shows that C, O, N, Co, Cu, and Fe elements were uniformly distributed on the electrode surface.

Transmission electron microscopy (TEM) was used to further characterize the catalysts on the electrode surface. The particle size of the  $\text{CuFe}_2\text{O}_4/\text{Cu}_2\text{O}/\text{Cu}$  catalyst derived from CuFe PBA was about 500 nm ([Fig. 2a](#)). TEM-EDS mapping ([Fig. 2b–g](#)) results show that the elements on  $\text{CuFe}_2\text{O}_4/\text{Cu}_2\text{O}/\text{Cu}$  particle surface were mainly C, O, N, Cu, and Fe. Furthermore, selected area electron diffraction (SAED) ([Fig. 2h](#)) analysis demonstrates the existence of Cu,  $\text{Cu}_2\text{O}$ , and  $\text{CuFe}_2\text{O}_4$  plane diffraction rings, indicating that the metal compounds on the catalysts consisted of Cu,  $\text{Cu}_2\text{O}$ , and  $\text{CuFe}_2\text{O}_4$ . These results are consistent with the X-ray diffraction (XRD) analysis discussed below. High-resolution TEM images shown in [Fig. S1](#) exhibit that the  $\text{CuFe}_2\text{O}_4/\text{Cu}_2\text{O}/\text{Cu}$  catalyst particles have a carbon coated structure.

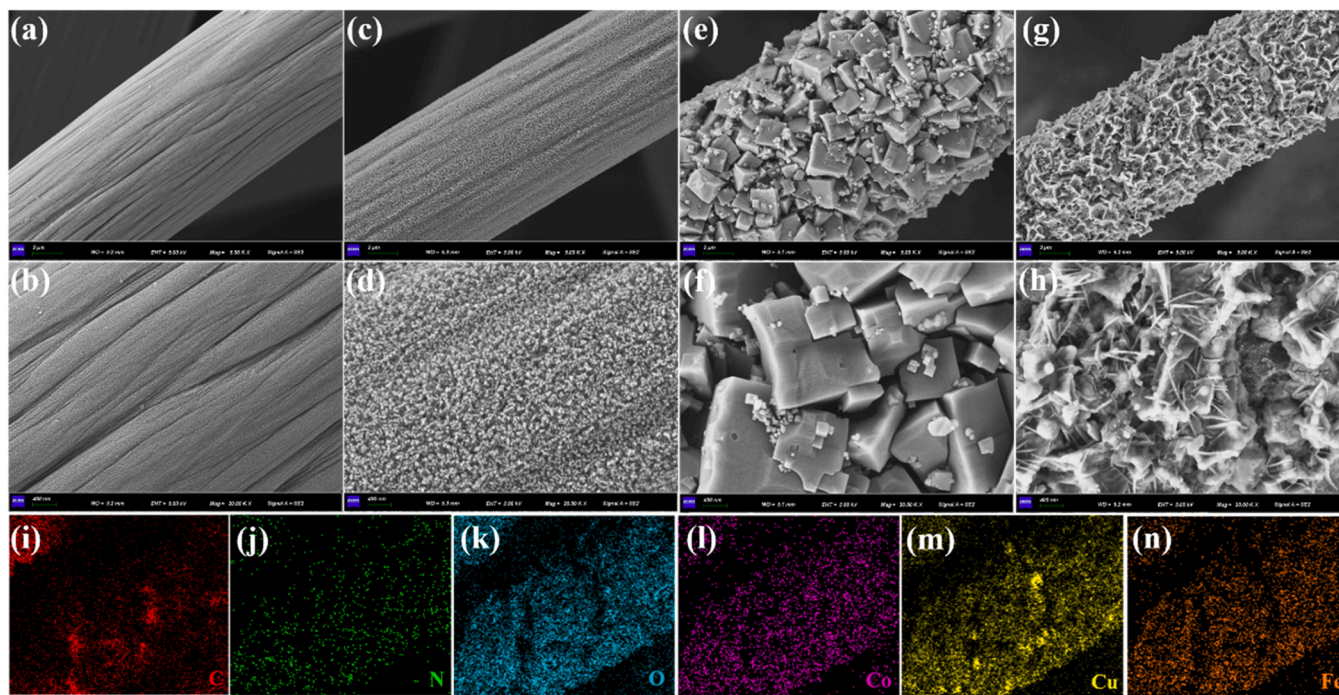


**Fig. 1.** SEM images of (a, b) RGF, (c, d) EGF, (e, f) CuFe PBA@EGF, and (g, h) CuFe<sub>2</sub>O<sub>4</sub>/Cu<sub>2</sub>O/Cu@EGF; and (i–n) elemental mapping images of CuFe<sub>2</sub>O<sub>4</sub>/Cu<sub>2</sub>O/Cu@EGF.

The phases on different GF electrodes were analyzed by XRD. Fig. 3a exhibits the XRD pattern of RGF, revealing the existence of two obvious diffraction peaks at 25° and 42°, representing graphitic carbon. After *in situ* etching with CoO<sub>x</sub>, the EGF electrode showed the characteristic peaks representing graphitic carbon as well as the characteristic peak of the Co<sub>3</sub>O<sub>4</sub> (311) crystal plane at 36.8°. After the growth of PBA at room temperature, distinct derivative peaks at 17.7°, 25.2°, 35.9°, 40.3°, and 51.7° appeared on the EGF electrode, respectively, ascribed to the (200), (220), (400), (420), and (440) crystal planes of CuFe PBA (JCPDS No. 86–0514). It indicates that CuFe PBA was successfully grown on the EGF surface. After the high-temperature calcination of CuFe PBA@EGF, the characteristic PBA peaks disappeared and new diffraction peaks were observed. The diffraction peaks at 43.3°, 50.4°, and 74.1° represented the (111), (200), and (220) crystal faces of Cu (JCPDS No. 04–0836), respectively. The diffraction peaks at 36.5°, 42.4°, and 61.5° represented the (111), (200), and (220) crystal faces of Cu<sub>2</sub>O (JCPDS No. 75–1531), respectively. The diffraction peaks at 18.3°, 30.2°, 35.5°, 53.6°, 57.1°, and 62.7° were ascribed to the (111), (220), (311), (422), (511), and (440) crystal faces of CuFe<sub>2</sub>O<sub>4</sub> (JCPDS No. 77–0010), respectively. These results indicate that CuFe PBA loaded on the electrode surface underwent decomposition and converted into Cu<sup>0</sup>, copper oxide, and iron oxide phases.

The chemical composition and surface electronic state of the electrode were characterized by X-ray photoelectron spectroscopy (XPS). The elements present on the RGF surface (Fig. S2) included C and O. The elements present on the surface of EGF (Fig. S3) were C, O, and Co. The elements on the surface of CuFe PBA@EGF (Fig. S4) were mainly C, O, N, Co, Cu, and Fe. After high-temperature carbonization of the electrode, the elements identified on the surface of CuFe<sub>2</sub>O<sub>4</sub>/Cu<sub>2</sub>O/Cu@EGF (Fig. 3b) were still C, O, N, Co, Cu, and Fe. The C 1s peak of the CuFe<sub>2</sub>O<sub>4</sub>/Cu<sub>2</sub>O/Cu@EGF electrode (Fig. 3c) was deconvoluted into three peaks at 284.7, 288.9, and 285.8 eV, which corresponded to C=C/C–C [33], C=O [34], and C–O [35], respectively. The O 1s peak of the CuFe<sub>2</sub>O<sub>4</sub>/Cu<sub>2</sub>O/Cu@EGF electrode (Fig. 3d) was deconvoluted into three peaks at 529.9, 530.8, and 532.2 eV, which corresponded to O–M [36], O=C [37], and O–C [38], respectively. The N 1s peak of the CuFe<sub>2</sub>O<sub>4</sub>/Cu<sub>2</sub>O/Cu@EGF electrode (Fig. 3e) showed a peak at 407 eV,

corresponding to nitrogen oxide. In the Fe 2p spectrum of the CuFe<sub>2</sub>O<sub>4</sub>/Cu<sub>2</sub>O/Cu@EGF electrode (Fig. 3f), the fitted peaks at 724.5 and 711.0 eV were ascribed to Fe<sup>3+</sup> [39,40]. In the Cu 2p spectrum of the CuFe<sub>2</sub>O<sub>4</sub>/Cu<sub>2</sub>O/Cu@EGF electrode (Fig. 3g), the fitted peaks at 934.5 and 954.6 eV were ascribed to Cu<sup>2+</sup> [41], while the fitted peaks at 933.4 and 953.0 eV were ascribed to Cu<sup>0</sup>/Cu<sup>+</sup> [42]. In the Cu 2p spectrum, the peaks of Cu<sup>+</sup> and Cu<sup>0</sup> were not easily separated due to their relatively close positions [43], thus the Cu LMM Auger spectrum was used to distinguish Cu<sup>+</sup> and Cu<sup>0</sup>. The fitted peaks at 916.8 and 918.6 eV were assigned to Cu<sup>+</sup> and Cu<sup>0</sup>, respectively [44]. These results indicate that the Cu on the CuFe<sub>2</sub>O<sub>4</sub>/Cu<sub>2</sub>O/Cu@EGF electrode mainly existed in three valence states; *i.e.*, Cu<sup>2+</sup>, Cu<sup>+</sup>, and Cu<sup>0</sup>.

The electrodes were further characterized by Raman spectroscopy. The peaks near 1350 and 1585 cm<sup>−1</sup> corresponded to the D band and G band of graphite, respectively. The D band corresponds to carbon with defects or a disordered structure and the G band corresponds to carbon with an ordered structure [45]. Therefore, the G band to D band peak intensity ratio (*I<sub>G</sub>/I<sub>D</sub>*) is used to evaluate the graphitization degree of carbon materials. Fig. 4a exhibits that the *I<sub>G</sub>/I<sub>D</sub>* ratios of RGF, EGF, and CuFe PBA@EGF were 0.89, 0.57, and 0.94, respectively. After high-temperature carbonization of CuFe PBA grown on the EGF electrode, the *I<sub>G</sub>/I<sub>D</sub>* ratio decreased from 0.94 to 0.73, indicating that CuFe PBA derivatives showed a lower degree of graphitization. A low degree of graphitization is favorable for the exposure of metal active centers [46]. Therefore, these results indicate that the CuFe<sub>2</sub>O<sub>4</sub>/Cu<sub>2</sub>O/Cu@EGF electrode, with highly exposed Cu and Fe active centers, was more conducive to the reaction of H<sub>2</sub>O<sub>2</sub> with these active centers capable of generating strong oxidizing radicals.

Fourier transform infrared (FTIR) spectroscopy was used to analyze the functional groups on the electrode. Fig. 4b illustrates that the FTIR spectrum of CuFe PBA@EGF shows absorption peaks at 595, 1612, and 2103 cm<sup>−1</sup>, attributed to Fe–C bending vibration, H–O–H bending, and CN stretching vibration combined with Cu atoms, respectively [47]. After the high-temperature calcination of the CuFe PBA@EGF electrode, the peaks related to the functional groups of CuFe PBA almost completely disappeared, and new absorption peaks appeared at other positions. The new adsorption peaks were located at 445, 467, and



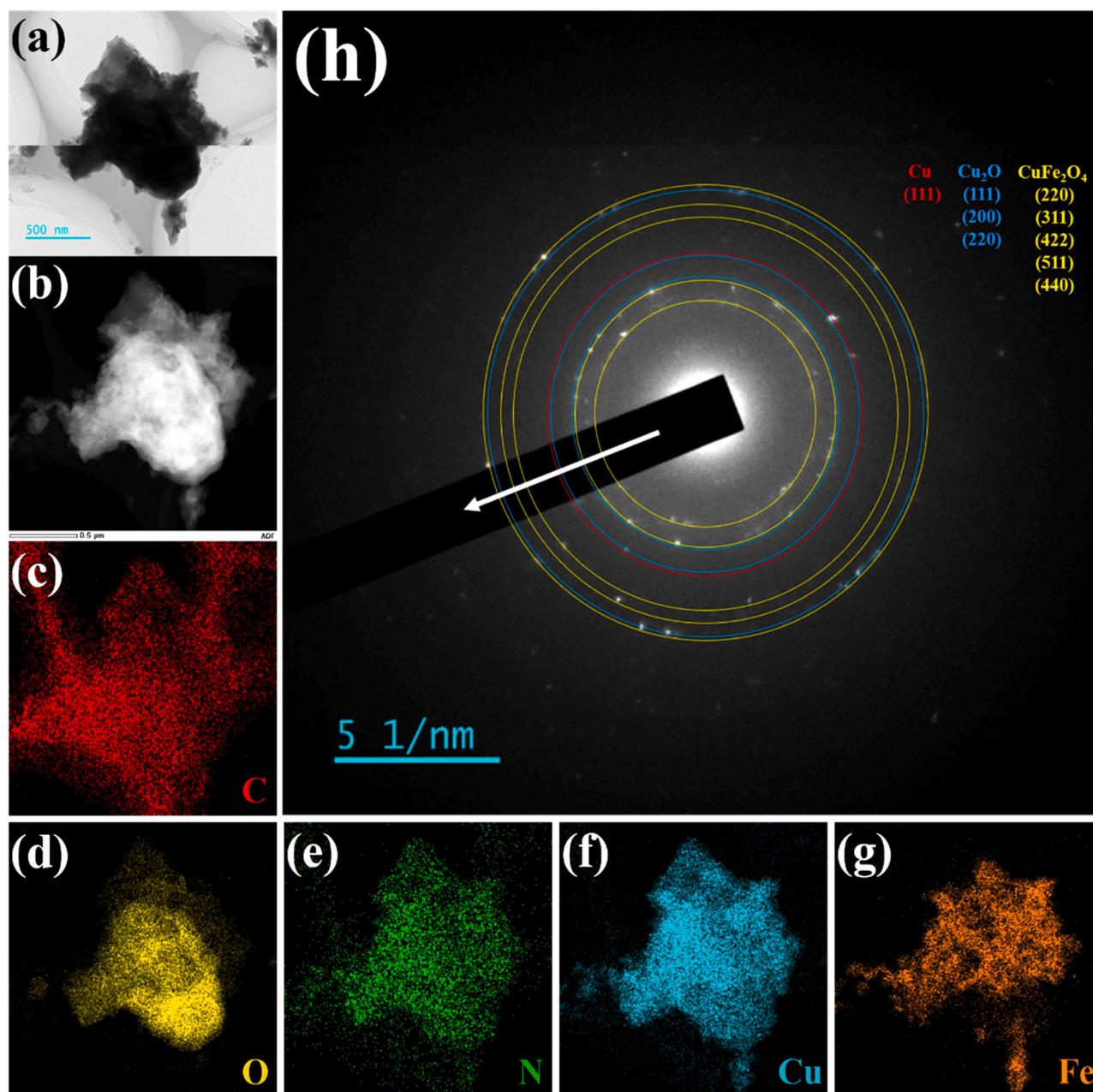


**Fig. 2.** (a) TEM image of CuFe<sub>2</sub>O<sub>4</sub>/Cu<sub>2</sub>O/Cu; (b–g) element mapping images of C, O, N, Cu, and Fe; and (h) SAED pattern of CuFe<sub>2</sub>O<sub>4</sub>/Cu<sub>2</sub>O/Cu.

585 cm<sup>-1</sup>, and these peaks were attributed to metal–oxygen stretching vibration [48–50]. The new adsorption peaks at 1340, 1380, and 1515 cm<sup>-1</sup> were attributed to C–O stretching vibration [51], –CH<sub>2</sub> bending vibration, and C=C stretching vibration [52], respectively.

The specific surface and pore size distribution of the GF electrode before and after modification were studied, and the corresponding results are shown in Fig. 4c and d. The specific surface area of RGF increased from 1.19 to 4.70 m<sup>2</sup>·g<sup>-1</sup> after *in situ* etching with CoO<sub>x</sub> because cobalt oxide underwent a series of redox reactions with carbon to form porous structures on the GF fiber surface, leading to a larger specific surface area. After the growth of CuFe PBA on the EGF electrode, the specific surface increased from 4.70 to 52.07 m<sup>2</sup>·g<sup>-1</sup>. Although the specific surface area of the electrode increased significantly after PBA growth on the EGF electrode surface, SEM analysis showed that a dense coating layer of CuFe PBA covered the EGF electrode. This dense structure was not conducive to O<sub>2</sub> reaching the surface of EGF for the 2e-ORR, because it could negatively affect the cathode performance. After

the high-temperature calcination of CuFe PBA@EGF, the specific surface area decreased from 52.07 to 3.68 m<sup>2</sup>·g<sup>-1</sup>. However, despite this decline in specific surface area, the CuFe<sub>2</sub>O<sub>4</sub>/Cu<sub>2</sub>O/Cu@EGF electrode consisted of many pore canals (see Fig. 1g and h) that could allow O<sub>2</sub> to reach the electrode surface, and the structure of the carbonized PBA was rougher and showed more exposed metal active sites. The pore size distribution diagram (Fig. 4d) illustrates that the pores of the CuFe<sub>2</sub>O<sub>4</sub>/Cu<sub>2</sub>O/Cu@EGF electrode prepared after *in situ* CoO<sub>x</sub> etching, *in situ* PBA growth, and high-temperature calcination consisted of a larger proportion of macropores, which was conducive to the transfer of O<sub>2</sub>, H<sub>2</sub>O<sub>2</sub>, and pollutants.

Noteworthy, the interfacial charge transfer resistance of an electrode material determines its electron transfer rate. Nyquist diagrams containing curves with smaller diameters indicate lower interfacial charge transfer resistance. The CuFe<sub>2</sub>O<sub>4</sub>/Cu<sub>2</sub>O/Cu@EGF electrode showed the smallest curve diameter (Fig. 5a), indicating that this electrode had a faster electron transfer rate. This was beneficial for increasing the



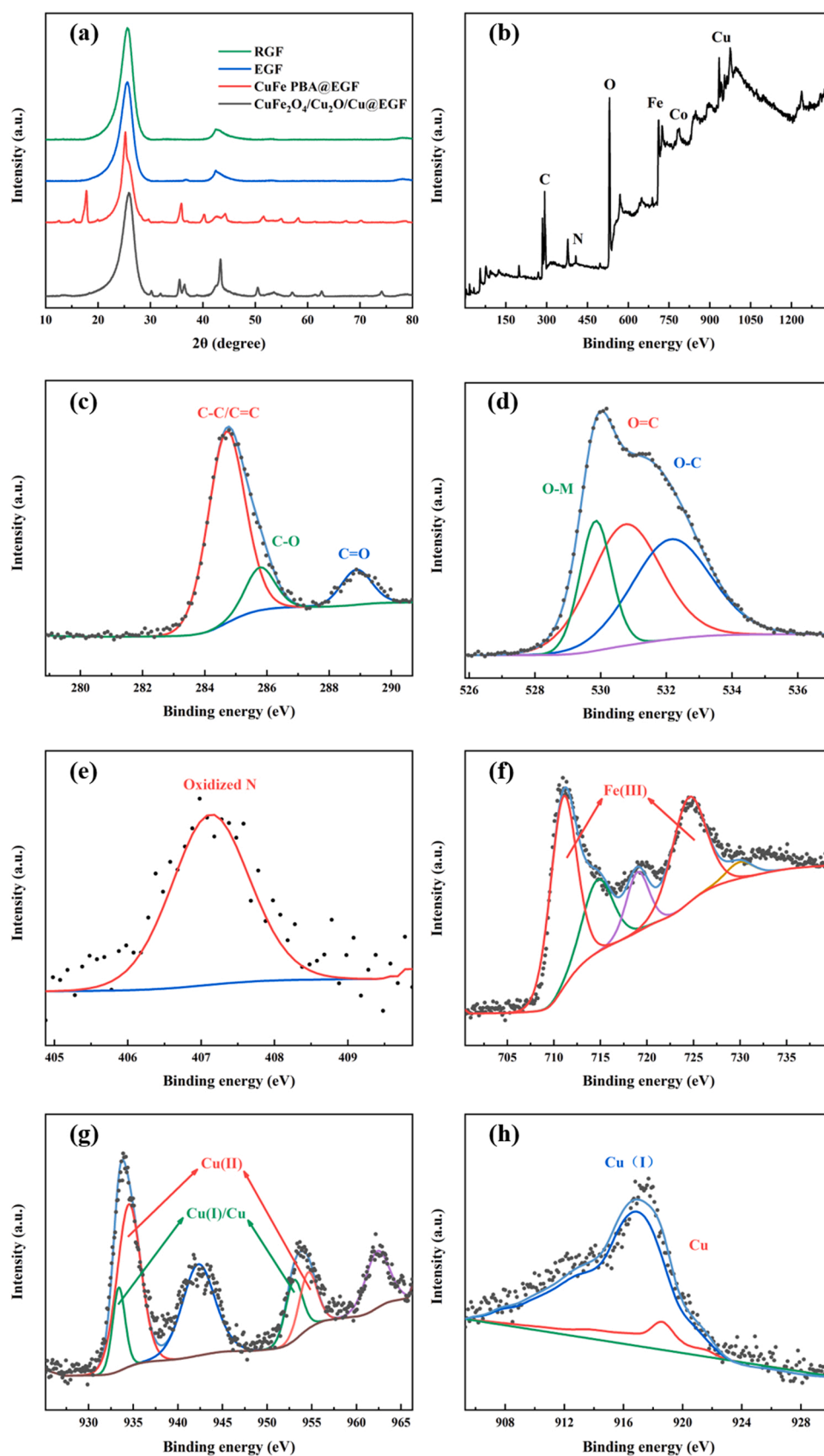


**Fig. 3.** (a) XRD patterns of RGF, EGF,  $\text{CuFe PBA}@EGF$ , and  $\text{CuFe}_2\text{O}_4/\text{Cu}_2\text{O}/\text{Cu}@EGF$ ; (b) XPS survey spectrum of  $\text{CuFe}_2\text{O}_4/\text{Cu}_2\text{O}/\text{Cu}@EGF$ ; high-resolution (c) C 1s, (d) O 1s, (e) N 1s, (f) Fe 2p, (g) Cu 2p, and (h) Cu LMM Auger XPS spectra of  $\text{CuFe}_2\text{O}_4/\text{Cu}_2\text{O}/\text{Cu}@EGF$ .

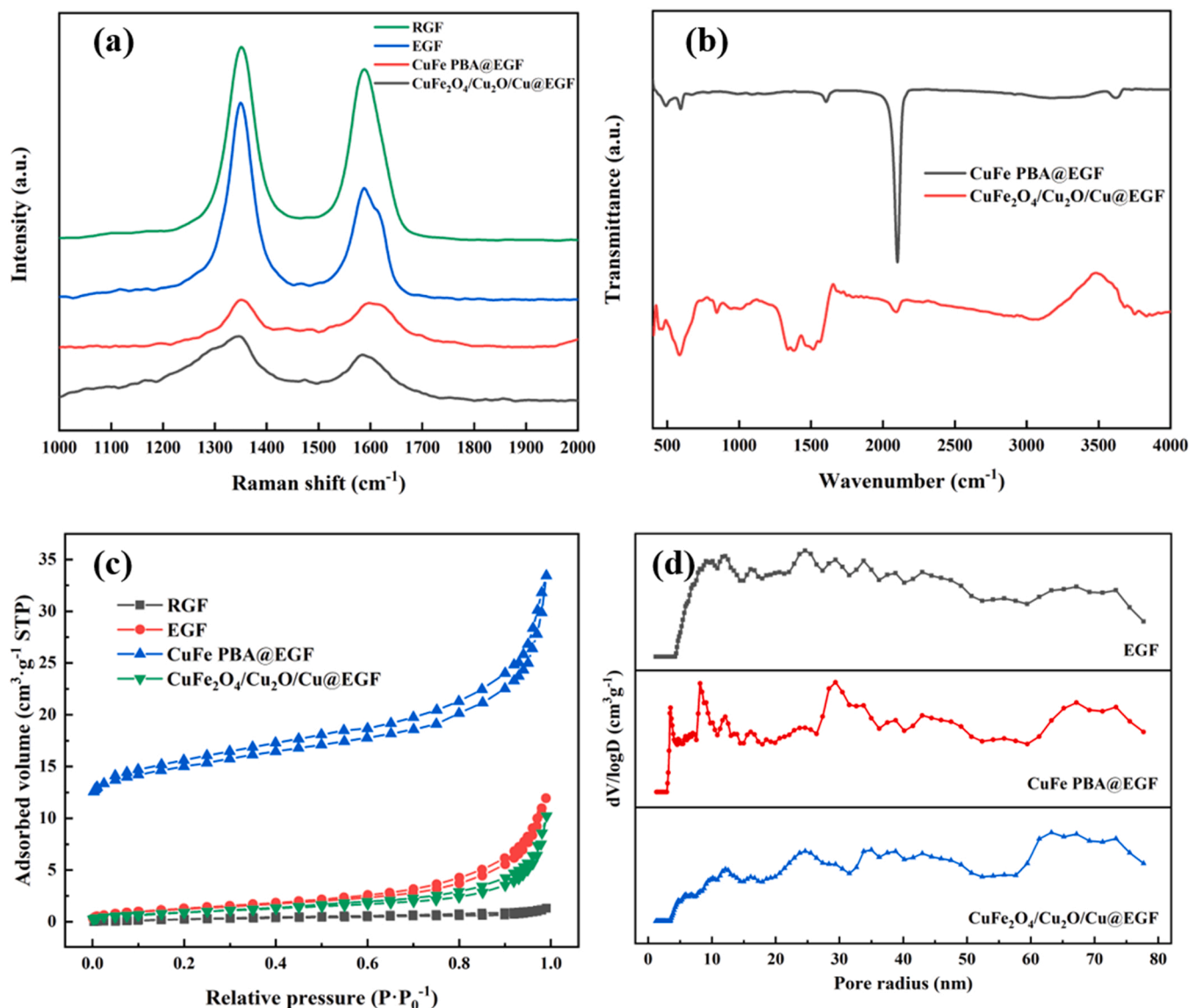


Fig. 4. (a) Raman spectra of different electrodes, (b) FTIR spectra of CuFe PBA@EGF and CuFe<sub>2</sub>O<sub>4</sub>/Cu<sub>2</sub>O/Cu@EGF, (c) N<sub>2</sub> adsorption–desorption isotherms of different electrodes, and (d) pore size distribution curves of different electrodes.

reaction rate of H<sub>2</sub>O<sub>2</sub> formation and activation.

The electrochemically active surfaces of the electrodes were measured by cyclic voltammetry (CV) tests in 10 mM K<sub>3</sub>[Fe(CN)<sub>6</sub>] and 100 mM KCl solution (Fig. 5b). The electroactive specific surface areas of RGF, EGF, CuFe PBA@EGF, and CuFe<sub>2</sub>O<sub>4</sub>/Cu<sub>2</sub>O/Cu@EGF, calculated by using the Randles–Sevcik equation [53], were 19.00, 54.20, 68.20, and 112.60 cm<sup>2</sup>, respectively. After *in situ* CoO<sub>x</sub> etching, CuFe PBA growth, and high-temperature calcination, the CuFe<sub>2</sub>O<sub>4</sub>/Cu<sub>2</sub>O/Cu@EGF electrode showed a larger electroactive area, which was conducive to providing more electroactive sites for the generation and activation of H<sub>2</sub>O<sub>2</sub>, thereby improving the *in situ* hetero-EF performance of this electrode.

The yield of H<sub>2</sub>O<sub>2</sub> on a cathode is an important parameter index in hetero-EF systems. The yield of H<sub>2</sub>O<sub>2</sub> on a cathode directly determines the yield of ·OH and other free radicals. However, it is difficult to directly measure the amount of H<sub>2</sub>O<sub>2</sub> produced within *in situ* hetero-EF systems. This is because the H<sub>2</sub>O<sub>2</sub> produced on a cathode can be directly activated by the catalyst on the cathode to generate free radicals in the system. Therefore, in this study, the electrocatalytic performance of electrodes to produce H<sub>2</sub>O<sub>2</sub> was indirectly studied by measuring the electron transfer number (*n*) for the reduction reaction of O<sub>2</sub> by rotating

ring disk electrode (RRDE) technique. Figs. S5 and 5d exhibit that the *n* values of RGF were 2.85–2.98 in the V/RHE range of –0.55 to –0.80, and the corresponding yields of H<sub>2</sub>O<sub>2</sub> were 57.26–50.98%. The *n* values of EGF were 2.49–2.68 at –0.55 to –0.80 V/RHE, and the corresponding yields of H<sub>2</sub>O<sub>2</sub> were 75.48–66.19%. The selectivity of H<sub>2</sub>O<sub>2</sub> after *in situ* CoO<sub>x</sub> etching modification of the GF electrode was significantly higher, which was due to the abundant porous structure and large electroactive area of EGF leading to enhanced H<sub>2</sub>O<sub>2</sub> production. The *n* values of EGF loaded with CuFe PBA were 2.93–3.08 at –0.55 to –0.80 V/RHE, and the corresponding yields of H<sub>2</sub>O<sub>2</sub> were 53.47–45.92%. After loading CuFe PBA on the EGF electrode, the yield of H<sub>2</sub>O<sub>2</sub> decreased significantly. This was mainly due to the formation of the dense CuFe PBA cladding on the surface of the EGF electrode, which made it difficult for O<sub>2</sub> to reach the EGF electrode for ORR. After high-temperature calcination, the *n* values of CuFe<sub>2</sub>O<sub>4</sub>/Cu<sub>2</sub>O/Cu@EGF were 2.45–2.55 at –0.55 to –0.80 V/RHE, and the corresponding yields of H<sub>2</sub>O<sub>2</sub> were 77.48–72.53%. This was because CuFe PBA was transformed into a rough and porous structure after calcination, which was conducive to the diffusion of O<sub>2</sub>. Moreover, the carbonization of the CuFe PBA structure also provided more active sites for O<sub>2</sub> to undergo 2e-ORR, which improved the H<sub>2</sub>O<sub>2</sub> yield in the CuFe<sub>2</sub>O<sub>4</sub>/Cu<sub>2</sub>O/Cu@EGF

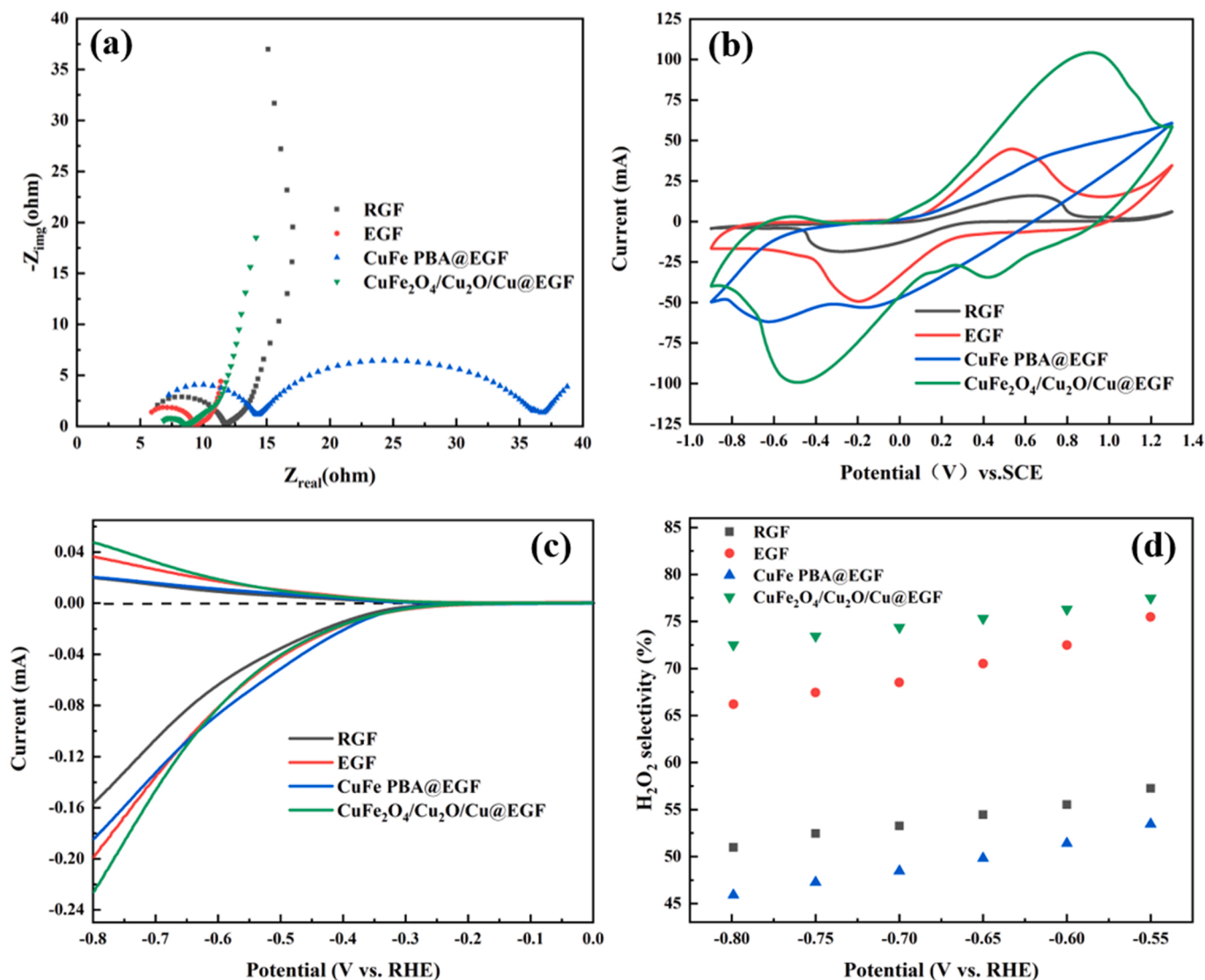


Fig. 5. (a) CV, (b) electrochemical impedance spectroscopy, (c) RRDE, and (d) H<sub>2</sub>O<sub>2</sub> selectivity of RGF, EGF, CuFe PBA@EGF, and CuFe<sub>2</sub>O<sub>4</sub>/Cu<sub>2</sub>O/Cu@EGF.

cathode.

### 3.2. Influences of experimental factors on SMX degradation

Degradation performance of the *in situ* hetero-EF system was mainly influenced by the electrode preparation conditions and the reaction conditions. In this study, the influences of calcination temperature and concentration of the CuFe PBA growth solution for the CuFe<sub>2</sub>O<sub>4</sub>/Cu<sub>2</sub>O/Cu@EGF electrode on the performance of the reaction system were investigated. The effects of reaction conditions such as the initial pH, current density, aeration rate, and rotational speed on the degradation performance of the system were also systematically investigated.

With increasing calcination temperature, the SMX removal efficiency of the CuFe<sub>2</sub>O<sub>4</sub>/Cu<sub>2</sub>O/Cu@EGF electrode first increased and then decreased (Fig. 6a). The SMX degradation efficiency was the lowest when the electrode calcination temperature was 300 °C. This was mainly because the CuFe PBA structure was not completely transformed into rough and porous CuFe oxide at this lower calcination temperature. This was not beneficial for the diffusion of O<sub>2</sub> to the EGF electrode surface for the production of H<sub>2</sub>O<sub>2</sub>. Moreover, the active Cu and Fe centers were not fully exposed at the lower calcination temperature, which was not conducive to the activation of H<sub>2</sub>O<sub>2</sub>. The highest SMX degradation efficiency was achieved at an electrode calcination

temperature of 500 °C, with  $94.68 \pm 1.33\%$  of the SMX removed in 45 min. The SMX removal efficiency of the CuFe<sub>2</sub>O<sub>4</sub>/Cu<sub>2</sub>O/Cu@EGF electrode declined when the calcination temperature exceeded 500 °C. This was potentially due to the severe damage to the catalyst structure caused by the high temperature, which was expected to reduce the number of catalytic active sites on the surface of the CuFe<sub>2</sub>O<sub>4</sub>/Cu<sub>2</sub>O/Cu@EGF electrode.

Fig. 6b demonstrates that with increasing concentration of CuFe PBA growth solution, the SMX removal efficiency of the CuFe<sub>2</sub>O<sub>4</sub>/Cu<sub>2</sub>O/Cu@EGF electrode showed a trend of first increasing and then decreasing. When the growth solution concentration was too low, the loading of catalyst on EGF was also lower, leading to a lower number of catalytic active sites on the surface of the CuFe<sub>2</sub>O<sub>4</sub>/Cu<sub>2</sub>O/Cu@EGF electrode. It indicates that less H<sub>2</sub>O<sub>2</sub> was activated to produce reactive oxygen species (ROS). When the concentration of growth solution was too high, the resulting excessively high catalyst loading on the EGF surface was not conducive to allowing the O<sub>2</sub> to reach the EGF surface through the catalytic layer of CuFe PBA derivatives. Therefore, the best SMX removal efficiency of  $97.13 \pm 0.60\%$  was achieved in 45 min with the CuFe<sub>2</sub>O<sub>4</sub>/Cu<sub>2</sub>O/Cu@EGF electrode prepared using a CuFe PBA growth solution concentration of 30 mM.

Fig. 6c illustrates that the SMX degradation efficiency of the composite electrode was the highest when the initial pH was 3, with 100% of



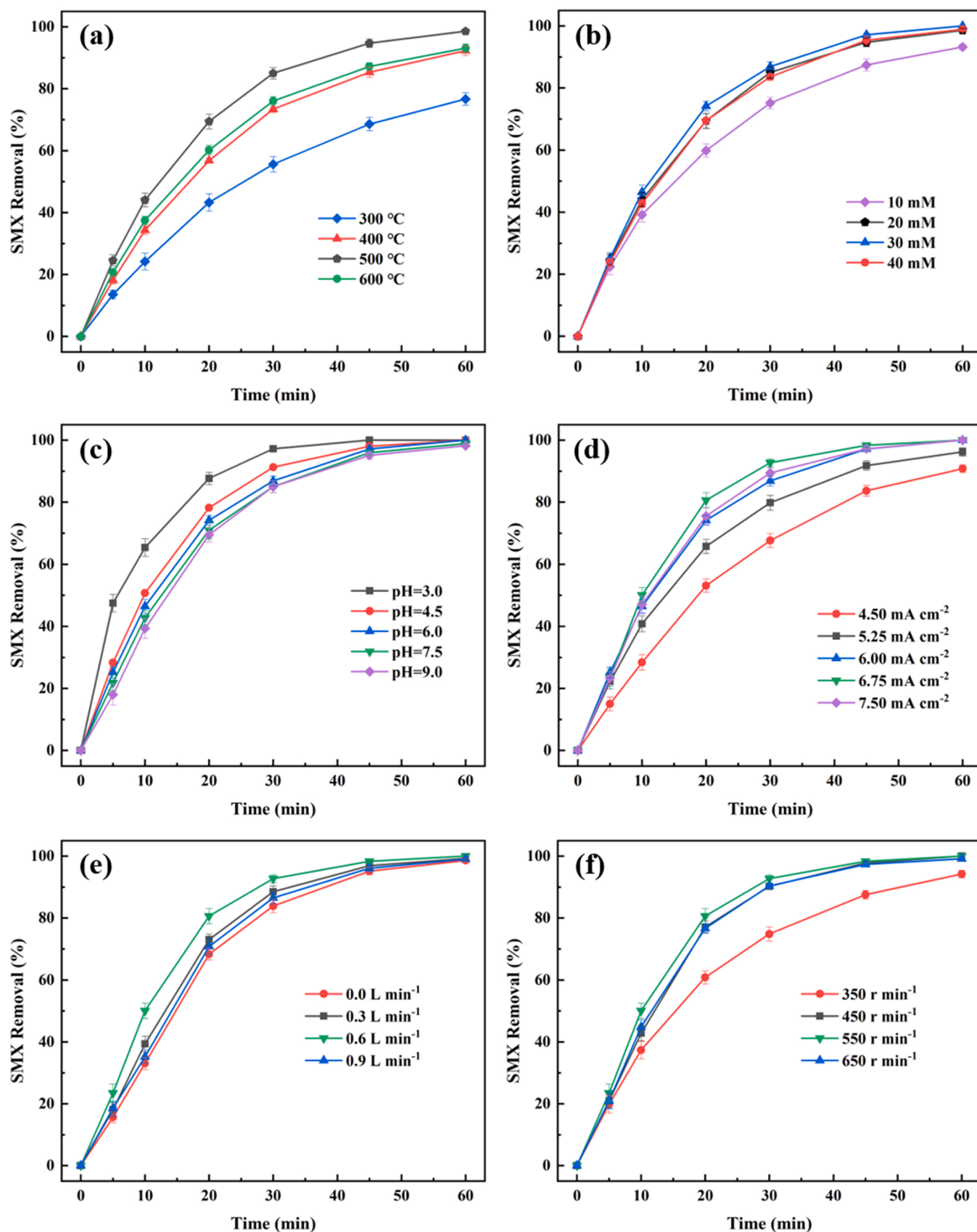


Fig. 6. Effects of (a) calcination temperature, (b)  $\text{CuFe}_2\text{O}_4/\text{Cu}_2\text{O}/\text{Cu@EGF}$  concentration, (c) initial pH of solution, (d) current density, (e) aeration rate, and (f) rotational speed on the removal of SMX by the  $\text{CuFe}_2\text{O}_4/\text{Cu}_2\text{O}/\text{Cu@EGF}$  electrode.

the SMX being removed in 45 min. This was mainly due to the favorable production of  $\text{H}_2\text{O}_2$  and the dissolution of some metal ions by the  $\text{CuFe}_2\text{O}_4/\text{Cu}_2\text{O}/\text{Cu@EGF}$  electrode under acidic conditions, which improved the degradation efficiency of the system. With increasing initial pH, the SMX degradation efficiency of the  $\text{CuFe}_2\text{O}_4/\text{Cu}_2\text{O}/\text{Cu@EGF}$  electrode gradually decreased. However, even at  $\text{pH} = 9$ , the SMX removal efficiency was still  $95.11 \pm 1.23\%$  within 45 min. It indicates that this composite electrode exhibited a good pH application range in the hetero-EF system. For ease of use in practical applications, a near-neutral initial pH ( $\text{pH} = 6$ ) was selected for the following experiment.

Fig. 6d exhibits that the SMX removal efficiency of the composite electrode gradually increased with the increase of current density in the range of  $4.5\text{--}6.75\text{ mA}\cdot\text{cm}^{-2}$ . This is attributed to the fact that a higher current density facilitated the generation of  $\text{H}_2\text{O}_2$  and promoted the valence state circulation of metal ions in the catalyst, which was conducive to the generation of strong oxidizing free radicals. When the current density was  $6.75\text{ mA}\cdot\text{cm}^{-2}$ , the highest SMX removal efficiency ( $98.32 \pm 0.71\%$  removed in 45 min) was achieved. However, the SMX removal efficiency declined when the current density was increased above  $6.75\text{ mA}\cdot\text{cm}^{-2}$ . This was mainly because an excessively high

current density led to the occupation of the active sites by side reactions such as hydrogen evolution and oxidation of  $\text{H}_2\text{O}_2$  [54], clearly indicating their unavailability for the generation and activation of  $\text{H}_2\text{O}_2$ .

Furthermore, Fig. 6e exhibits that with increasing aeration rate, the SMX removal efficiency of the  $\text{CuFe}_2\text{O}_4/\text{Cu}_2\text{O}/\text{Cu@EGF}$  electrode first increased and then decreased. The highest SMX removal efficiency was achieved under an aeration of  $0.6\text{ L}\cdot\text{min}^{-1}$ . However, even in the absence of aeration, the  $\text{CuFe}_2\text{O}_4/\text{Cu}_2\text{O}/\text{Cu@EGF}$  electrode still achieved good SMX removal performance. This was mainly due to the fact that the solution itself contained dissolved  $\text{O}_2$  from the oxygen evolution reaction of the anode as well as the air. When the aeration rate was increased to  $0.9\text{ L}\cdot\text{min}^{-1}$ , the SMX removal efficiency decreased mainly because excessive aeration led to a large number of bubbles in the reaction solution, which increased the mass transfer resistance of the reaction solution. Under a constant current, this higher mass transfer resistance led to an increase in the reaction voltage, which promoted side reactions on the electrode. Thus, the degradation performance of the system was reduced.

The SMX removal efficiency of the composite electrode increased with increasing rotational speed within a certain rotational speed range (Fig. 6f). This is attributed to the fact that higher rotational speeds

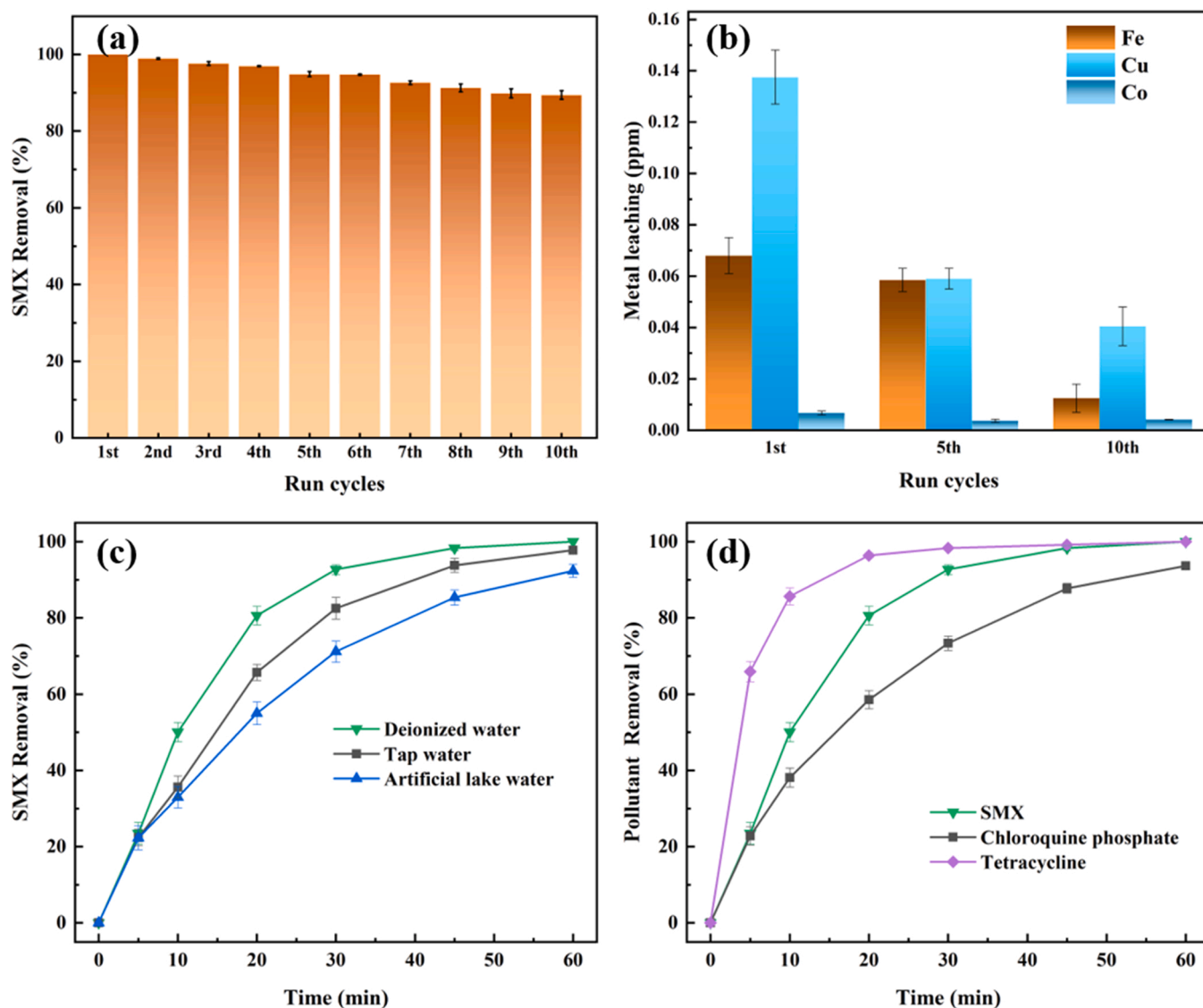


Fig. 7. Performance of the  $\text{CuFe}_2\text{O}_4/\text{Cu}_2\text{O}/\text{Cu@EGF}$  electrode: (a) stability across 10 cycles, (b) metal ion leaching in the hetero-EF system, (c) effect of water quality conditions, and (d) removal efficiency for other pollutants. Conditions:  $6.75\text{ mA}\cdot\text{cm}^{-2}$ ,  $20\text{ mg}\cdot\text{L}^{-1}$  SMX,  $0.6\text{ L}\cdot\text{min}^{-1}$  aeration rate,  $\text{pH} = 6.0$ .

enabled the rapid transfer of O<sub>2</sub> and SMX in the reaction solution to the electrode surface. The best SMX removal efficiency was achieved at the rotational speed of 550 rpm. With the increase in the rotational speed above 550 rpm, the SMX removal efficiency decreased. This was potentially due to the following reasons: 1) Insufficient contact between the dissolved O<sub>2</sub> and the reaction site on the electrode surface due to the excessive rotation speed; and 2) Insufficient contact between the strong oxidizing free radicals and SMX.

### 3.3. Properties of the composite cathode

The stable operation of the composite cathode was directly related to its performance in the system. When this electrode was continuously used for 10 cycles (Fig. 7a), with a performance decline of only 10.58 ± 1.11%, it showed good stability. Moreover, SEM and XPS results of CuFe<sub>2</sub>O<sub>4</sub>/Cu<sub>2</sub>O/Cu@EGF electrode were compared after one cycle and 10 cycles. The characterization results of SEM and XPS indicate that, compared with the composite electrode used for one time, the morphology of the composite electrode after 10-times use did not show any obvious changes, and there was still a rough and multi-slit CuFe<sub>2</sub>O<sub>4</sub>/Cu<sub>2</sub>O/Cu catalytic layer on the electrode surface (Fig. S6). Moreover, the types and contents of elements on the composite electrode did not change much, maintaining a relatively stable state (Fig. S7 and Table S1). This was also the reason why the composite cathode still showed a high electrocatalytic degradation performance after repeated use.

*In situ* hetero-EF cathode materials contain metal compounds that activate H<sub>2</sub>O<sub>2</sub> to generate strong oxidizing free radicals, and the dissolution of these metal ions in the reaction solution during operation is inevitable. If the concentration of metal ions dissolved in the reaction solution is very high, secondary pollution of the wastewater occurs, and the stability of the electrode gets reduced. Therefore, the metal ions leached from the electrode in the reuse process were studied. Fig. 7b demonstrates that after repeated use of the CuFe<sub>2</sub>O<sub>4</sub>/Cu<sub>2</sub>O/Cu@EGF electrode for 10 cycles, the Cu, Fe, and Co concentrations leached from the electrode were only 0.041 ± 0.007, 0.013 ± 0.006, and 0.004 ± 0.000 mg·L<sup>-1</sup>, respectively. All these concentrations are lower than Chinese national wastewater drainage standards GB 13456–2012 and GB 25467–2010.

The SMX removal efficiency of the composite electrode was also investigated under different water quality conditions. Simulated wastewaters containing SMX prepared with deionized water, tap water, and artificial lake water were used for these degradation experiments. Fig. 7c illustrates that compared with the simulated wastewater prepared with deionized water, the SMX removal efficiencies in the simulated wastewaters prepared with tap water and artificial lake water were lower. The most significant decline was observed in the simulated wastewater prepared with artificial lake water. This was due to the presence of organic substances in the artificial lake water and tap water (Table S2), which competed with SMX to consume strong oxidizing free radicals.

Besides the SMX removal, the removal of the composite electrode for different pollutants was also studied. Tetracycline and chloroquine

phosphate were selected as the target pollutants, the concentration of degraded pollutants was 20 mg·L<sup>-1</sup>. Chloroquine phosphate is considered to be a clinically effective drug for the treatment of pneumonia and has been widely used in the past few years [55]. Fig. 7d illustrates that the CuFe<sub>2</sub>O<sub>4</sub>/Cu<sub>2</sub>O/Cu@EGF electrode showed good degradation efficiency for both tetracycline and chloroquine phosphate. Therefore, this electrode presented good universality for the degradation of different pollutants.

Moreover, compared with other related literature reports (Table 1), the CuFe<sub>2</sub>O<sub>4</sub>/Cu<sub>2</sub>O/Cu@EGF electrode showed excellent degradation performance for the removal of pollutants. The unit energy consumption of TOC degradation in the *in situ* hetero-EF system was calculated. According to formula S3 and the degradation of TOC (Fig. S8), the unit energy consumption of the system for TOC degradation was 1.35 kWh·g<sup>-1</sup> TOC. The energy consumption result was compared with the unit energy consumption reported in the literature, and the result is presented in Table S3. The *in situ* heterogeneous electrochemical Fenton oxidation degradation system also offers certain advantages in energy consumption.

### 3.4. Mechanism analysis

Fig. 8a shows that H<sub>2</sub>O<sub>2</sub> alone does not exhibit degradation effect on SMX because of the low oxidation ability of H<sub>2</sub>O<sub>2</sub> and limited ability to oxidize SMX. In a hetero-EF system with no applied voltage, the CuFe<sub>2</sub>O<sub>4</sub>/Cu<sub>2</sub>O/Cu@EGF cathode showed a certain SMX adsorption effect. The adsorption saturation state was reached in 20 min, with 20.83 ± 1.27% of the SMX being adsorbed. The absorption of SMX by the composite electrode was conducive to the reaction of SMX with the strong oxidizing free radicals generated on the surface of the electrode, thus improving the degradation efficiency of the cathode. Although this adsorbed SMX was not degraded in the absence of an applied voltage, applying a voltage later would lead to SMX degradation. The SMX removal efficiency under anodic oxidation reached 56.37 ± 1.61% within 60 min. After switching to the composite cathode, the SMX removal efficiency reached 100.00% within 60 min. This was due to the ability of the CuFe<sub>2</sub>O<sub>4</sub>/Cu<sub>2</sub>O/Cu@EGF cathode to generate and activate H<sub>2</sub>O<sub>2</sub>, leading to the generation of strong oxidizing free radicals.

The free radicals in the reaction system were identified by electron paramagnetic resonance (EPR), and 5,5-dimethyl-1-pyrroline-N-oxide (DMPO) and 2,2,6,6-tetramethylpiperidine (TMPO) were used as free radical trapping agents. Fig. 8b demonstrates that strong signals with intensity ratios of 1:2:2:1, 1:1:1:1, and 1:1:1 were observed, indicating that ·OH, superoxide anions (·O<sub>2</sub><sup>-</sup>), and singlet oxygen (<sup>1</sup>O<sub>2</sub>) were mainly present in the system.

The contribution of several free radicals to SMX degradation was studied. Compared to other free radicals, hydroxyl free radicals have a very short lifetime. In the reaction system, ·OH was primarily generated on the electrode. It was difficult for the ·OH produced on the electrode surface to travel long distances to the solution, thus hydrophobic nitrobenzene (NB) was selected as the ·OH quencher on the surface of the electrode. In contrast, hydrophilic tert-butyl alcohol (TBA) was selected as the quencher of ·OH in solution (as opposed to the ·OH

**Table 1**  
Degradation performance of different electrode materials in hetero-EF processes.

Cathode	Reaction condition				Removal efficiency	Ref.
	Volume of solution (mL)	Concentration of SMX (mg·L <sup>-1</sup> )	Current density or voltage	pH		
AD-Fe/3DPC	100	20	3.75 mA·cm <sup>-2</sup>	3	81.3% (200 min)	[56]
CoFe-NC	100	10	- 0.7 V/SCE	1	91.0% (300 min)	[57]
FeOx/NHPC750	100	50	12.5 mA·cm <sup>-2</sup>	6	95.0% (90 min)	[58]
Ce/Fe@NPC-GF	100	20	2.0 mA·cm <sup>-2</sup>	3	100.0% (120 min)	[59]
ChiSuc	100	20	6.0 mA·cm <sup>-2</sup>	7	70.0% (60 min)	[60]
γ-FeOOH GPCA	500	25.3	12.5 mA·cm <sup>-2</sup>	natural	99.9% (120 min)	[61]
Cu-Fe <sub>2</sub> O <sub>3</sub> /EGF	300	20	6.0 mA·cm <sup>-2</sup>	6	100.0% (90 min)	[62]
CuFe <sub>2</sub> O <sub>4</sub> /Cu <sub>2</sub> O/Cu@EGF	300	20	6.75 mA·cm <sup>-2</sup>	6	100.0% (60 min)	This study



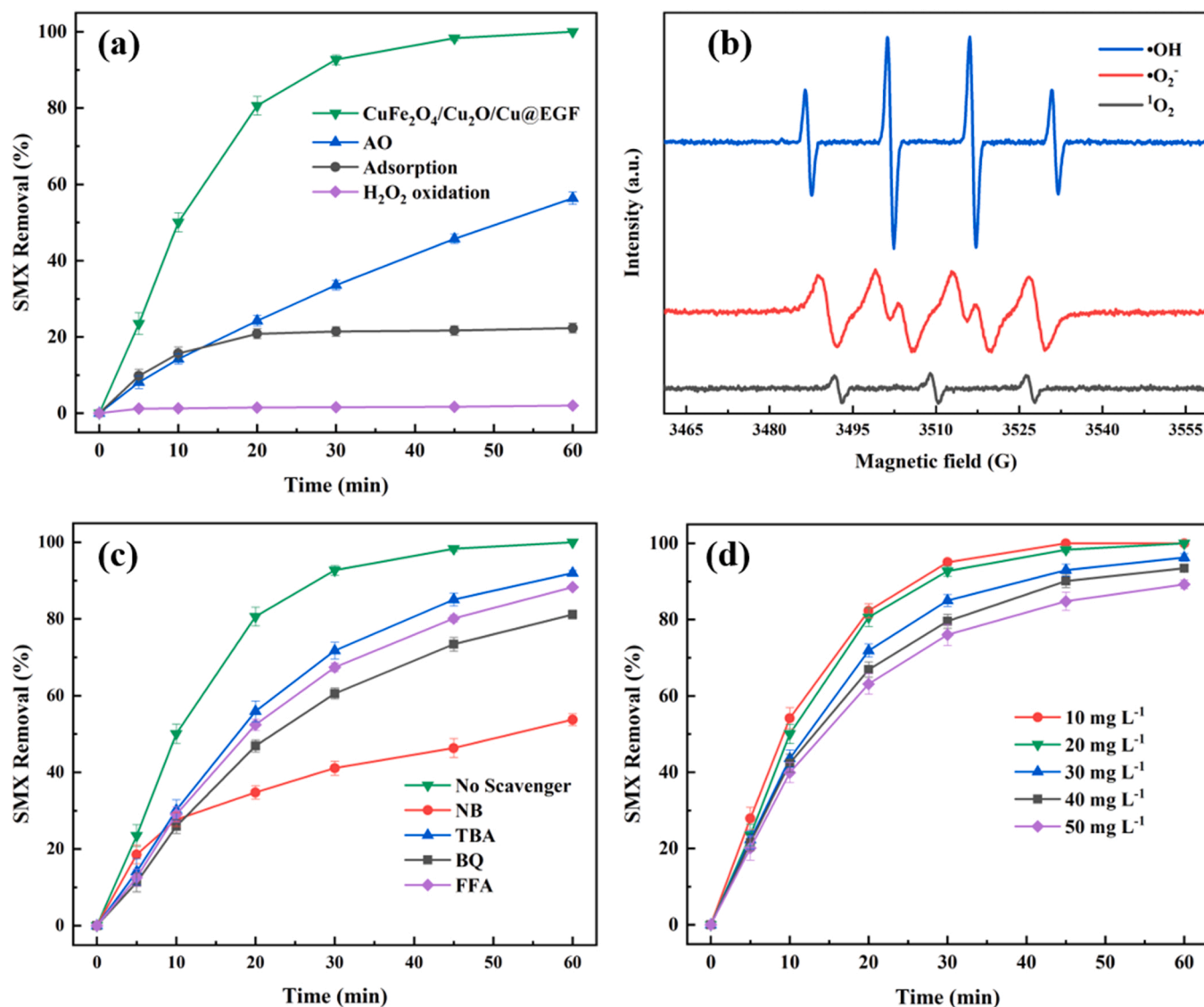


Fig. 8. (a) Performance of different systems for the removal of SMX, (b) DMPO and TMPO spin-trapping EPR spectra, (c) free radical scavengers, and (d) the effect of different initial SMX concentrations on the removal of SMX.

adsorbed on the electrode surface). Benzoquinone (BQ) was used as the quencher of  $\cdot\text{O}_2^-$ , and furfuryl alcohol (FFA) was used as the quencher of  $^1\text{O}_2$ . After adding NB, TBA, BQ, and FFA to the system (Fig. 8c), the SMX removal efficiency decreased by  $51.99 \pm 1.74$ ,  $13.25 \pm 0.97$ ,  $24.92 \pm 107$ , and  $18.19 \pm 0.24\%$  after 45 min, respectively. The addition of the  $\cdot\text{OH}$  quenchers (NB and TBA) most significantly inhibited the degradation of SMX, indicating that  $\cdot\text{OH}$  played a major role in SMX degradation. In this system, the  $\cdot\text{OH}$  was mainly adsorbed on the cathode surface after the *in situ* activation of  $\text{H}_2\text{O}_2$  produced on the cathode surface. Moreover,  $\cdot\text{O}_2^-$  and  $^1\text{O}_2$  in the system also degraded SMX. There were two main sources of the  $\cdot\text{O}_2^-$  produced in the system: 1) the  $\cdot\text{O}_2^-$  generated by  $\text{O}_2$  by obtaining an electron on the cathode; 2) the  $\cdot\text{O}_2^-$  generated by  $\text{H}_2\text{O}_2$  reacting with  $\text{Fe}^{3+}$  and  $\text{Cu}^{2+}$ . The generation of  $^1\text{O}_2$  in the system was potentially because some of the produced  $\cdot\text{OH}$  did not have enough time to contact and react with SMX. Consequently, this  $\cdot\text{OH}$  spontaneously reacted or reacted with  $\cdot\text{O}_2^-$  to generate  $^1\text{O}_2$ . Fig. 8d exhibits that with increasing initial SMX concentration, the SMX degradation efficiency of the system did not clearly decline. This was because the higher concentration of SMX led to a greater chance of contact with the hydroxyl free radicals generated on the electrode, thus reducing the conversion of hydroxyl free radicals into  $^1\text{O}_2$ . Attributed to this

mechanism, the removal efficiency of pollutants in this system did not decrease significantly with increasing pollutant concentration.

Based on the obtained results, a mechanism for the generation of free radicals was proposed. First, two reaction paths were observed for  $\text{O}_2$  at the cathode: 1)  $\text{O}_2$  gained an electron at the cathode to form  $\cdot\text{O}_2^-$ ; 2)  $\text{O}_2$  underwent 2e-ORR to produce  $\text{H}_2\text{O}_2$ . The electrocatalytically produced  $\text{H}_2\text{O}_2$  was rapidly transferred to the exposed active metal sites on the electrode, where it was activated to form  $\cdot\text{OH}$ . The  $\cdot\text{OH}$  in solution existed for a relatively short time due to the rapid contact reaction with organic pollutants. Compared with  $\cdot\text{OH}$ , the  $^1\text{O}_2$  existed in solution for a longer time. The  $\cdot\text{OH}$  that did not react with pollutants was eventually converted to  $^1\text{O}_2$ , which had a longer lifetime. The  $\cdot\text{OH}$ ,  $\cdot\text{O}_2^-$ , and  $^1\text{O}_2$  species eventually mineralized the pollutants into carbon dioxide, water, and inorganic salts. Furthermore, the high-valence metal ions ( $\text{Fe}^{3+}$  and  $\text{Cu}^{2+}$ ) generated after the activation of  $\text{H}_2\text{O}_2$  were reduced to low-valence metal ions ( $\text{Fe}^{2+}$  and  $\text{Cu}^+$ ) by the reduction of the cathode. The standard redox potential of  $\text{Fe}^{3+}/\text{Fe}^{2+}$  (0.77 V) was greater than that of  $\text{Cu}^{2+}/\text{Cu}^+$  (0.17 V), thus  $\text{Fe}^{3+}$  was able to be reduced by  $\text{Cu}^+$  to form  $\text{Fe}^{2+}$ .

### 3.5. DFT calculations of electrode

The formation of  $\text{H}_2\text{O}_2$  from  $\text{O}_2$  and the activation of  $\text{H}_2\text{O}_2$  into ROS mainly occurred in the prepared  $\text{CuFe}_2\text{O}_4/\text{Cu}_2\text{O}/\text{Cu}@EGF$  electrode. In general, the adsorption characteristics of  $\text{O}_2$  and  $\text{H}_2\text{O}_2$  on the surface of a cathode are very important for the occurrence of the 2e-ORR process. Therefore, the corresponding crystal plane structures of RGF, RGF-C, and EGF were constructed (Fig. 9), and the adsorption characteristics of  $\text{O}_2$  and  $\text{H}_2\text{O}_2$  on the electrode were studied by density functional theory (DFT) calculations. The O doping sites in the EGF structure may mainly exist in the C defect sites. Four O-doped structures were selected to investigate the O doping sites (Fig. S9). Table S4 presents that the third type of O-doped GF crystal plane structure shows the lowest total energy and forms the most stable structure, and thus it was selected as the crystal plane structure of EGF. Table 2 summarizes the adsorption energies ( $E_{\text{ads}}$ ) of  $\text{O}_2$  and  $\text{H}_2\text{O}_2$  on RGF, RGF-C, and EGF. Compared with RGF and RGF-C, EGF with C defects and O doping showed the smallest  $\text{O}_2$  adsorption energy. This result indicates that EGF was more conducive to the adsorption of  $\text{O}_2$ , which contributed to ORR. The adsorption energy of  $\text{H}_2\text{O}_2$  on EGF was 0.272 eV, which was higher than that of  $\text{H}_2\text{O}_2$  on RGF (0.263 eV). It indicates the lower adsorption force between  $\text{H}_2\text{O}_2$  and EGF. Therefore, the  $\text{H}_2\text{O}_2$  generated on the EGF electrode was able to desorb from the electrode surface, avoiding further reduction to  $\text{H}_2\text{O}$ .

In general, proper adsorption energy is essential for the subsequent activation of  $\text{H}_2\text{O}_2$  and the degradation of pollutants. The  $\text{H}_2\text{O}_2$  and SMX adsorption behavior of the  $\text{CuFe}_2\text{O}_4/\text{Cu}_2\text{O}/\text{Cu}$  catalyst derived from CuFe PBA and the  $\text{Fe}_3\text{O}_4$  derived from FeFe PBA were therefore studied. Table 3 presents that the  $E_{\text{ads}}$  of  $\text{Cu}_2\text{O}$  and  $\text{CuFe}_2\text{O}_4$  for  $\text{H}_2\text{O}_2$  in the  $\text{CuFe}_2\text{O}_4/\text{Cu}_2\text{O}/\text{Cu}$  catalyst were much lower than that of  $\text{Fe}_3\text{O}_4$  for  $\text{H}_2\text{O}_2$ , indicating that the  $\text{CuFe}_2\text{O}_4/\text{Cu}_2\text{O}/\text{Cu}$  catalyst showed a strong adsorption capacity for  $\text{H}_2\text{O}_2$ . This facilitated the  $\text{H}_2\text{O}_2$  activation process after  $\text{H}_2\text{O}_2$  adsorption on the catalyst.

Compared with the O–O bond of free  $\text{H}_2\text{O}_2$  (1.482 Å), the O–O bonds of  $\text{H}_2\text{O}_2$  adsorbed on the  $\text{CuFe}_2\text{O}_4/\text{Cu}_2\text{O}/\text{Cu}$  and  $\text{Fe}_3\text{O}_4$  catalysts were elongated during the adsorption process. This O–O bond was more elongated by  $\text{Cu}_2\text{O}$  and the Cu active components in the  $\text{CuFe}_2\text{O}_4/\text{Cu}_2\text{O}/\text{Cu}$  catalyst. It indicates that the  $\text{CuFe}_2\text{O}_4/\text{Cu}_2\text{O}/\text{Cu}$  catalyst would more significantly promote the dissociation of  $\text{H}_2\text{O}_2$  to  $\cdot\text{OH}$ . According to the free radical quenching results, the active groups of the electrode mainly included  $\cdot\text{OH}$  on the electrode surface. Therefore, the adsorption behavior of SMX molecules on the electrode was particularly important. Table 3 presents that the adsorption energy of SMX on  $\text{CuFe}_2\text{O}_4$  in the  $\text{CuFe}_2\text{O}_4/\text{Cu}_2\text{O}/\text{Cu}$  catalyst was much lower than that of SMX on  $\text{Fe}_3\text{O}_4$ . It implies that  $\text{CuFe}_2\text{O}_4$  in  $\text{CuFe}_2\text{O}_4/\text{Cu}_2\text{O}/\text{Cu}$  catalyst was more likely to adsorb SMX on the catalyst surface, thus facilitating the reaction of  $\cdot\text{OH}$  and SMX on the catalyst surface.

Based on this analysis, it was concluded that the reaction occurred on  $\text{CuFe}_2\text{O}_4/\text{Cu}_2\text{O}/\text{Cu}$  catalyst. First, the  $\text{H}_2\text{O}_2$  generated on the EGF

**Table 2**

Absorption of  $\text{O}_2$  and  $\text{H}_2\text{O}_2$  on RGF, RGF-C, and EGF.

	RGF	RGF-C	EGF
$\Delta E_{\text{ads}}$ of $\text{O}_2$ (eV)	− 0.145	− 0.964	− 3.31
$\Delta E_{\text{ads}}$ of $\text{H}_2\text{O}_2$ (eV)	0.263	0.270	0.272

**Table 3**

Absorption and O–O bond length of  $\text{H}_2\text{O}_2$  on Cu (111),  $\text{Cu}_2\text{O}$  (111),  $\text{CuFe}_2\text{O}_4$  (311), and  $\text{Fe}_3\text{O}_4$  (222) surfaces.

	Cu (111)	$\text{Cu}_2\text{O}$ (111)	$\text{CuFe}_2\text{O}_4$ (311)	$\text{Fe}_3\text{O}_4$ (222)
O–O bond length (Å)	1.515	1.550	1.495	1.496
$\Delta E_{\text{ads}}$ of $\text{H}_2\text{O}_2$ (eV)	0.111	− 1.226	− 1.489	− 0.118
$\Delta E_{\text{ads}}$ of SMX (eV)	− 0.694	− 1.228	− 1.750	− 1.337

electrode surface was adsorbed on the surface of the  $\text{CuFe}_2\text{O}_4/\text{Cu}_2\text{O}/\text{Cu}$  catalyst by  $\text{CuFe}_2\text{O}_4$  and  $\text{Cu}_2\text{O}$ . Then, the O–O bond of the  $\text{H}_2\text{O}_2$  adsorbed on the catalyst was elongated due to the effect of  $\text{Cu}_2\text{O}$  and Cu, which was conducive to the activation of  $\text{H}_2\text{O}_2$  for the generation of  $\cdot\text{OH}$ . The SMX molecules in solution were adsorbed on the catalyst surface by  $\text{CuFe}_2\text{O}_4$ , where they reacted with  $\cdot\text{OH}$  generated on the catalyst surface. Thus, the degradation of SMX was realized. The  $\text{CuFe}_2\text{O}_4/\text{Cu}_2\text{O}/\text{Cu}@EGF$  electrode showed a better electrocatalytic degradation performance than the  $\text{Fe}_3\text{O}_4 @EGF$  electrode (Fig. S10) because various components of the catalyst played their respective roles.

### 3.6. Degradation pathways

In order to better understand the possible bond-breaking position of SMX during degradation, DFT calculations were used to calculate the bond dissociation energy (BDE) of each bond in the SMX molecule. Fig. 10b reveals that the smallest BDE was required for  $\text{N}_{16}-\text{O}_{17}$ , which required only 32.3 kcal·mol<sup>−1</sup> to break. Other common single bonds, such as  $\text{S}_6-\text{N}_5$ ,  $\text{C}_9-\text{S}_6$ ,  $\text{N}_5-\text{H}_{22}$ ,  $\text{C}_2-\text{O}_{17}$ ,  $\text{C}_1-\text{H}_{20}$ , and  $\text{H}_{26}-\text{N}_{13}$  bonds, showed BDE values below 90 kcal·mol<sup>−1</sup>. However, the  $\text{C}_4-\text{C}_3$  single bond exhibited the highest BDE (124.6 kcal·mol<sup>−1</sup>) among the single bonds of the SMX molecule, indicating that the  $\text{C}_4-\text{C}_3$  bond was not easily broken by attack. Furthermore, bonds such as  $\text{C}_{11}=\text{C}_{10}$ ,  $\text{S}_6=\text{O}_8$ ,  $\text{C}_4=\text{N}_{16}$ , and  $\text{C}_3=\text{C}_2$  were all double bonds with higher BDE values, and these bonds were generally difficult to break.

Based on the DFT calculations of the Fukui function, the attack sites of the SMX molecule by active species were predicted, and the degradation pathways of SMX in the hetero-EF system were accurately proposed. Fig. 10d–f show electron density isosurface mapping of the SMX molecular surface based on the Fukui function, in which red and blue, respectively, indicate positive and negative values, and the depth of color indicates the magnitude. Regions with larger positive values were

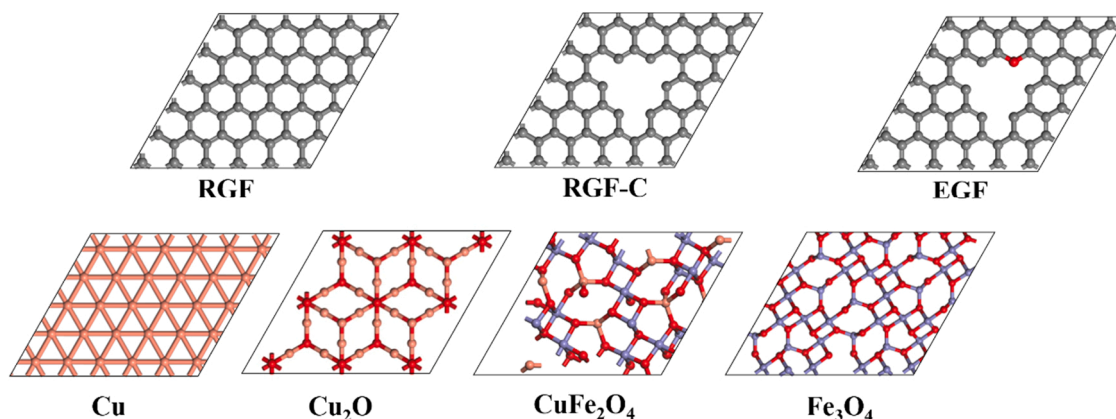


**Fig. 9.** Unit cell structures of RGF, RGF-C, EGF, Cu (111),  $\text{Cu}_2\text{O}$  (111),  $\text{CuFe}_2\text{O}_4$  (311), and  $\text{Fe}_3\text{O}_4$  (222).

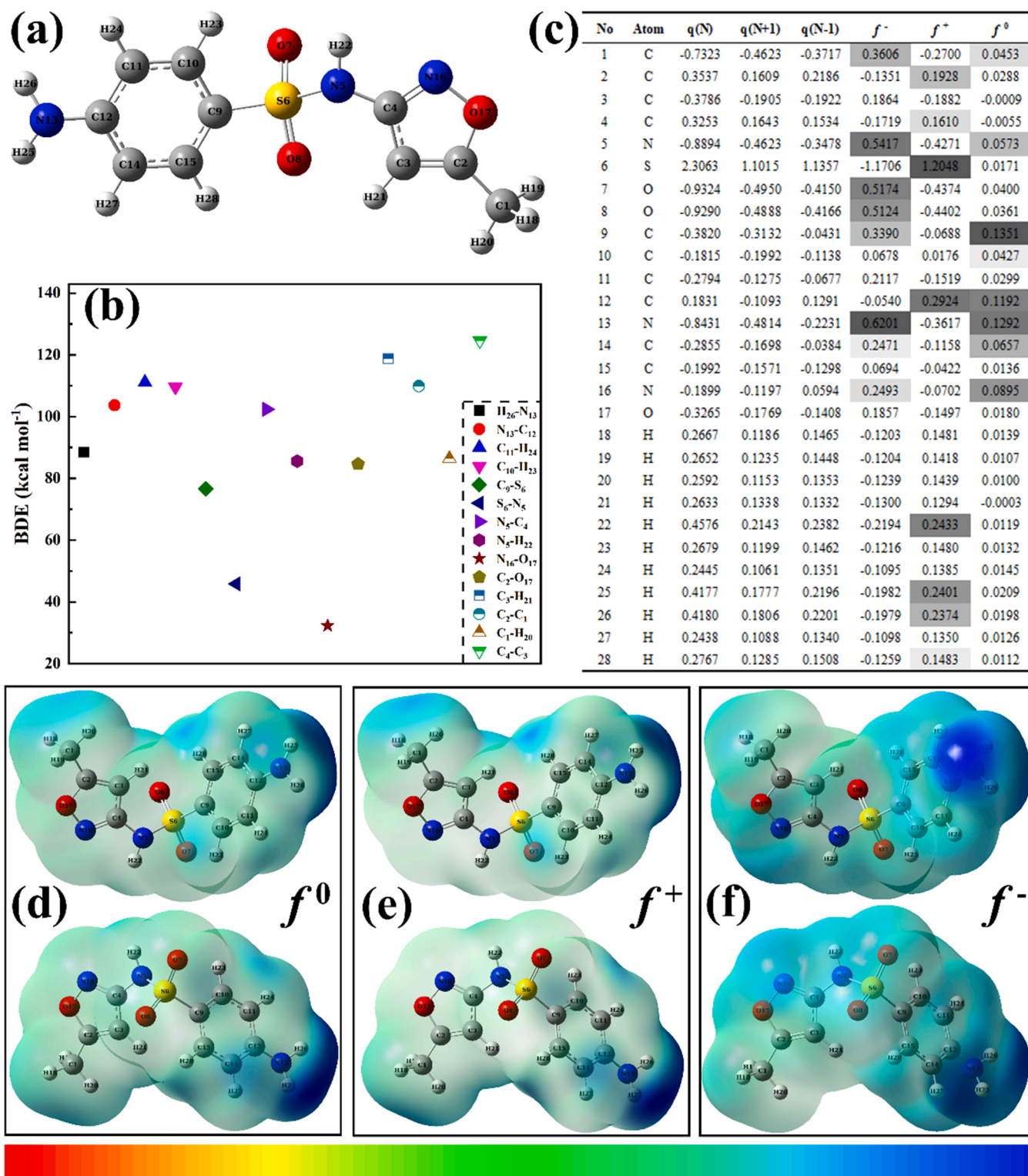


**Fig. 10.** (a) SMX molecular structure, (b) BDE values of each bond in the SMX molecule, (c) NPA charge distribution and condensed Fukui index of SMX, and the electron density isosurface mapping of (d)  $f^0$ , (e)  $f^+$ , and (f)  $f^-$ .

more likely to be active species attack sites. According to the electron density isosurface mapping of  $f^-$ ,  $f^+$ , and  $f^0$  for the SMX molecular surface, the aniline group in SMX was more reactive than the oxazole ring group and the sulfonamide group. Moreover, the bluest area was near the amino group of the aniline group, indicating that this site was the most active site for electrophilic, nucleophilic, and free radical reactions. Notably, it was difficult to quantitatively analyze the value of

the Fukui function by electron density isosurface mapping; therefore, a more concise and intuitive simplified Fukui function was used to predict the active species attack sites of the SMX molecule. According to the condensed Fukui function theory, higher  $f^-$ ,  $f^+$ , and  $f^0$  values indicate that atoms are more vulnerable to attacks by electrophilic species, nucleophilic species, and free radical species, respectively [63,64]. According to the condensed Fukui function calculation results shown in



Fig. 10c, the N<sub>7</sub>, C<sub>14</sub>, C<sub>8</sub>, C<sub>13</sub>, and C<sub>12</sub> positions in the SMX molecule exhibited high  $f^-$  values, indicating that these sites were more vulnerable to attack by  $^1\text{O}_2$ . N<sub>7</sub>, C<sub>14</sub>, C<sub>8</sub>, C<sub>13</sub>, and C<sub>12</sub> showed high  $f^+$  values, indicating that these sites were more vulnerable to attack by  $\cdot\text{O}_2^-$ . The high  $f^0$  values of N<sub>7</sub>, C<sub>14</sub>, C<sub>8</sub>, C<sub>13</sub>, and C<sub>12</sub> indicated that these sites were more vulnerable to the attack by  $\cdot\text{OH}$ .

Mass spectrometry analysis and DFT calculations were employed to identify the intermediate products produced during the SMX degradation, and the probable degradation pathways were proposed. The intermediate products produced during the SMX degradation are listed in Table S5. Fig. 11 exhibits the presence of seven main degradation pathways of SMX in the system. Pathway I: N<sub>15</sub> in the SMX molecule showed high  $f^-$  and  $f^0$  values, thus the bonds around the N<sub>15</sub> position were vulnerable to attack by free radicals and  $^1\text{O}_2$ . Moreover, the N<sub>16</sub>–O<sub>17</sub> bond exhibited the minimum BDE. Therefore, this bond was easily attacked and broken by  $\cdot\text{OH}$  and  $^1\text{O}_2$ . In addition to the breaking of the N<sub>16</sub>–O<sub>17</sub> bond, a substitution reaction of the methyl group with the hydroxyl group at position C<sub>2</sub> and a hydrogenation reaction also occurred to form P262. Pathway II: C<sub>9</sub> showed high  $f^-$  and  $f^0$  values, thus the bonds around the C<sub>9</sub> position were vulnerable to attack by free radicals and  $^1\text{O}_2$ . Furthermore, the C<sub>9</sub>–S<sub>6</sub> bond showed a low BDE; as a result, this bond was easily attacked by  $\cdot\text{OH}$  and  $^1\text{O}_2$  and broken to form P94 and P163. Next, the aniline bond of P94 was broken to form P94–1, which was oxidized to form P108. P163 was transformed into P137 after a series of reactions including S=O bond breaking on the sulfonyl group, N–S bond breaking, and hydroxylation. Pathway III: P258 was formed through the bond breaking of N<sub>16</sub>–O<sub>17</sub> (with the minimum BDE) and hydrogenation. Pathway IV: the bond around N<sub>5</sub> (N<sub>5</sub>–C<sub>4</sub>) was easily attacked and broken by  $\cdot\text{OH}$  and  $^1\text{O}_2$  to form P173. Pathway V: SMX was transformed into P218 after a series of reactions including bond breaking, hydroxylation, and hydrogenation on the oxazole ring of SMX. Pathway VI: S<sub>6</sub> showed a high  $f^+$  value and N<sub>5</sub> exhibited a high  $f^-$  value, thus the bonds around the S<sub>6</sub> and N<sub>5</sub> positions were vulnerable to attack by  $\cdot\text{O}_2^-$  and  $^1\text{O}_2$ , respectively. Moreover, the N<sub>5</sub>–S<sub>6</sub> bond exhibited a low BDE value, indicating that it was easily attacked and broken by  $\cdot\text{O}_2^-$  and  $^1\text{O}_2$  to form P158 and P99. The aniline bond of P158 was broken to form P143, and a series of reactions including N–S bond breaking occurred on

the oxazole ring of P99 to generate P101. Pathway VII: SMX was transformed into P300 through oxidation and hydroxylation reaction. Finally, the intermediates were eventually mineralized as CO<sub>2</sub>, H<sub>2</sub>O, and inorganic salts.

Noteworthy, it is important to investigate the toxicity of intermediate products to determine whether the treated wastewater can be discharged into the water environment or the sewage network. The theoretical values of acute and chronic toxicity of the intermediate products to three common aquatic organisms were calculated through Ecological Structure Activity Relationships. Fig. 12 illustrates that most of the intermediate products exhibited less chronic and acute toxicity than SMX. Although the chronic and acute toxicity of P94–1, P94, and P99 were stronger than that of SMX, it was expected that these slightly more toxic intermediate products would be converted to the less toxic intermediate products, namely, P108 and P101, with the progress of the degradation reaction. Moreover, growth inhibition experiments with *Chlorella* and *Escherichia coli* (*E. coli*) were used to evaluate the overall biotoxicity of the prepared catalyst during degradation. Fig. 13a demonstrates that as the degradation process proceeded, the inhibition of *E. coli* growth by the degradation solution gradually decreased. *E. coli* growth was no longer inhibited after 90 min Fig. 13b shows the growth inhibition of *Chlorella* using the degradation solution. The degradation solution did not inhibit the growth of *Chlorella* after 30 min. These results indicate that the system could effectively reduce the toxicity of SMX.

#### 4. Conclusions

A hetero-EF system was constructed to degrade SMX using the CuFe<sub>2</sub>O<sub>4</sub>/Cu<sub>2</sub>O/Cu@EGF electrode as the cathode. Under the conditions of pH = 6 and 6.75 mA·cm<sup>-2</sup>, 20 mg·L<sup>-1</sup> SMX was completely degraded within 60 min. Metal ion leaching from the electrode during the degradation process was very low. Furthermore, after 10 cycles of continuous use, the electrode maintained strong electrocatalytic activity, with the pollutant removal efficiency still reaching 89.42 ± 1.11% in 60 min. In addition to SMX degradation, the electrode also showed good degradation efficiency for tetracycline and chloroquine phosphate.

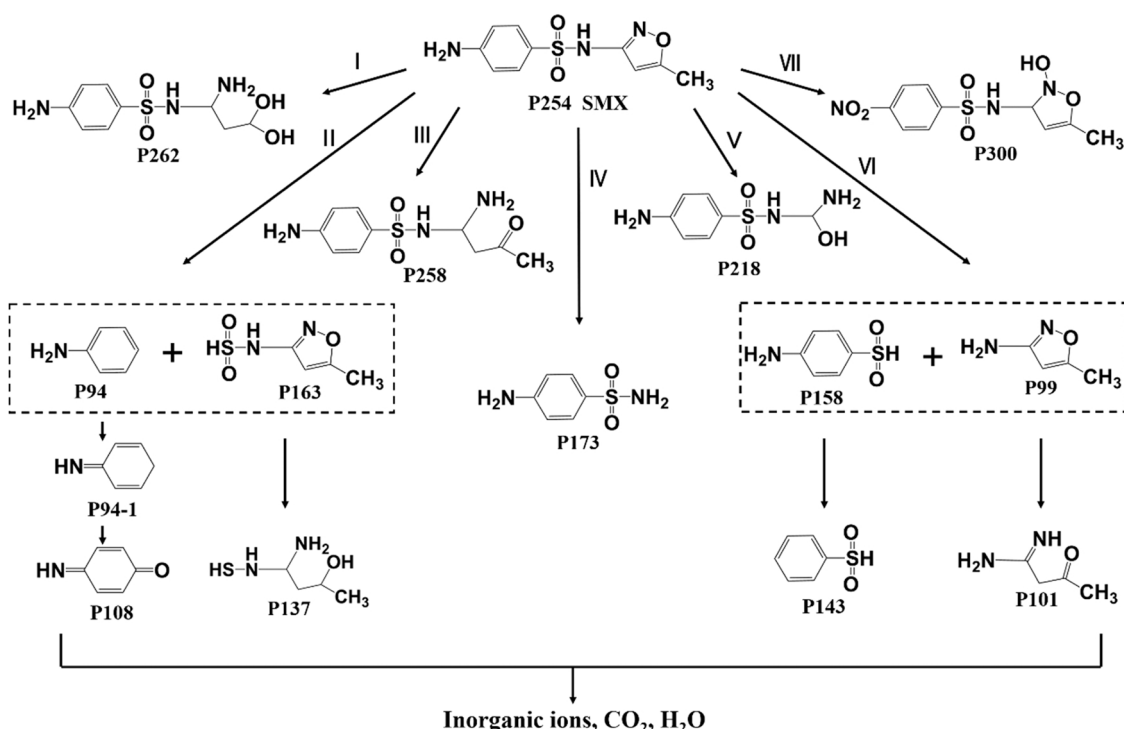


Fig. 11. Degradation pathways of SMX in the hetero-EF system.

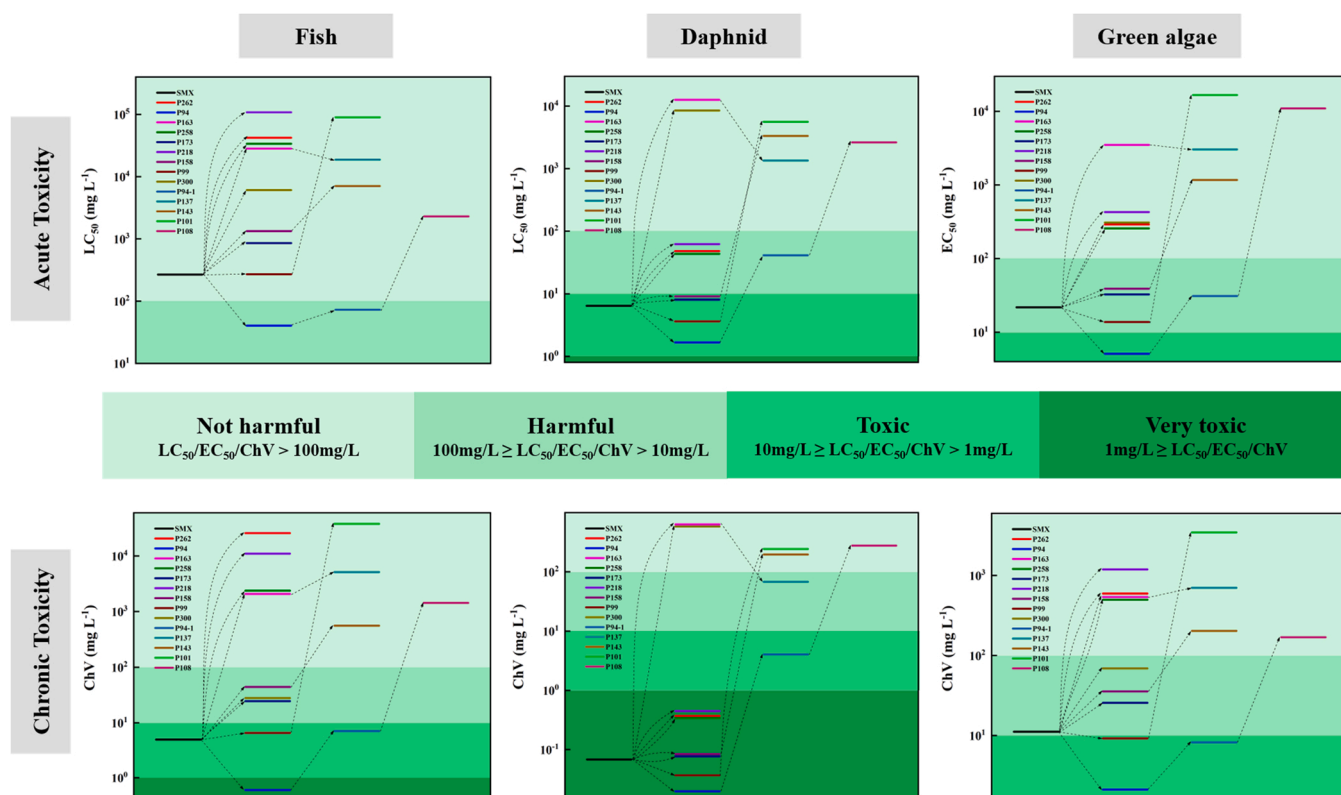


Fig. 12. Theoretically calculated acute and chronic toxicity of SMX and its degradation products.

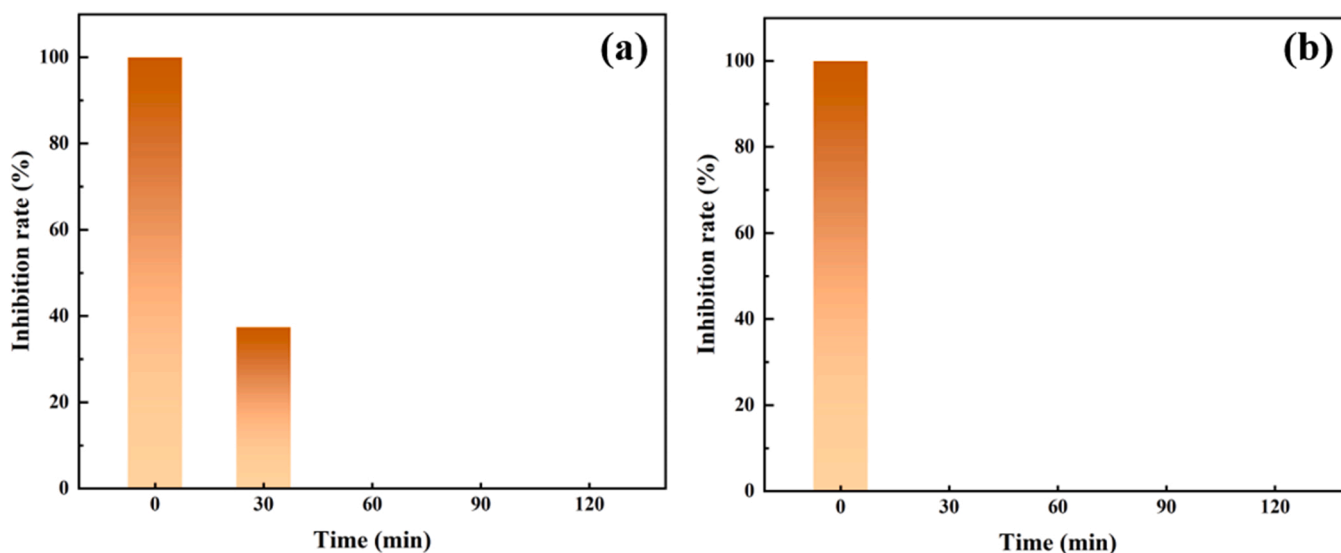


Fig. 13. Inhibition rates of (a) *E. coli* and (b) *Chlorella*.

Quenching experiments and EPR results showed that the active substances involved in degradation were  $\cdot\text{OH}$ ,  $\cdot\text{O}_2^-$ , and  $^1\text{O}_2$ , and the main active species was  $\cdot\text{OH}$ . According to DFT calculations and liquid quality detection, 14 possible intermediates and 7 SMX degradation pathways were proposed for this hetero-EF system. ECOSAR software and growth inhibition experiments with *E. coli* and *Chlorella* showed that the system reduced the biotoxicity of SMX. This study provides new insight into the safe and efficient treatment of pollutants in wastewater.

#### CRediT authorship contribution statement

**Haiqiang Qi:** Conceptualization, Methodology, Data curation, Formal analysis, Writing – original draft, Writing – review & editing. **Xuelin Shi:** Investigation, Software, Validation. **Zhirong Sun:** Formal analysis, Supervision. **Zhibin Liu:** Investigation, Software, Validation. **Zhirong Sun:** Formal analysis, Supervision. **Zihao Yan:** Investigation, Software, Validation. **Zhirong Sun:** Formal analysis, Supervision.

## Declaration of Competing Interest

The authors declare that they have no known competing financial interests or personal relationships that could have appeared to influence the work reported in this paper.

## Data Availability

Data will be made available on request.

## Acknowledgements

This work was supported by the National Natural Science Foundation of China (Grant No. 52070005).

## Appendix A. Supporting information

Supplementary data associated with this article can be found in the online version at [doi:10.1016/j.apcatb.2023.122722](https://doi.org/10.1016/j.apcatb.2023.122722).

## References

- [1] M. Nawaz, A. Shahzad, K. Tahir, J. Kim, M. Moztahida, J. Jang, M.B. Alam, S.-H. Lee, H.-Y. Jung, D.S. Lee, Photo-Fenton reaction for the degradation of sulfamethoxazole using a multi-walled carbon nanotube-NiFe<sub>2</sub>O<sub>4</sub> composite, *Chem. Eng. J.* 382 (2020), 123053.
- [2] M. Fatehifar, S.M. Borghei, Application of moving bed biofilm reactor in the removal of pharmaceutical compounds (diclofenac and ibuprofen), *J. Environ. Chem. Eng.* 6 (2018) 5530–5535.
- [3] H. Dong, Y. Fu, P. Wang, W. Jiang, G. Gao, X. Zhang, Degradation of chloramphenicol by Ti/PbO<sub>2</sub>-La anodes and alteration in bacterial community and antibiotics resistance genes, *Environ. Pollut.* 301 (2022), 119031.
- [4] X. Zhang, B. Xu, S. Wang, X. Li, C. Wang, Y. Xu, R. Zhou, Y. Yu, H. Zheng, P. Yu, Carbon nitride nanotubes anchored with high-density CuNx sites for efficient degradation of antibiotic contaminants under photo-Fenton process: performance and mechanism, *Appl. Catal. B: Environ.* 306 (2022), 121119.
- [5] Y. Zhou, C. Zhang, D. Huang, W. Wang, Y. Zhai, Q. Liang, Y. Yang, S. Tian, H. Luo, D. Qin, Structure defined 2D Mo<sub>2</sub>C/2D g-C<sub>3</sub>N<sub>4</sub> Van der Waals heterojunction: oriented charge flow in-plane and separation within the interface to collectively promote photocatalytic degradation of pharmaceutical and personal care products, *Appl. Catal. B: Environ.* 301 (2022), 120749.
- [6] A.A. Nada, B.O. Orimolade, H.H. El-Maghrabi, B.A. Koiki, M. Rivallin, M. F. Bekheet, R. Viter, D. Damberg, G. Lesage, I. Iatsunskyi, Photoelectrocatalysis of paracetamol on Pd-ZnO/N-doped carbon nanofibers electrode, *Appl. Mater. Today* 24 (2021), 101129.
- [7] X. Li, K. Liang, B. Yang, K. Xiao, H. Duan, G. Song, H. Zhao, Preparation and application of a targeted magnetically separated catalyst for sulfonamides degradation based on molecular dynamics selection and mechanism analysis, *Chem. Eng. J.* 432 (2022), 134365.
- [8] C. Gadipelly, A. Pérez-González, G.D. Yadav, I. Ortiz, R. Ibáñez, V.K. Rathod, K. V. Marathe, Pharmaceutical industry wastewater: review of the technologies for water treatment and reuse, *Ind. Eng. Chem. Res.* 53 (2014) 11571–11592.
- [9] Y. Song, J. Tian, S. Gao, P. Shao, J. Qi, F. Cui, Photodegradation of sulfonamides by g-C<sub>3</sub>N<sub>4</sub> under visible light irradiation: effectiveness, mechanism and pathways, *Appl. Catal. B: Environ.* 210 (2017) 88–96.
- [10] Z. Luo, M. Liu, D. Tang, Y. Xu, H. Ran, J. He, K. Chen, J. Sun, High H<sub>2</sub>O<sub>2</sub> selectivity and enhanced Fe<sup>2+</sup> regeneration toward an effective electro-Fenton process based on a self-doped porous biochar cathode, *Appl. Catal. B: Environ.* 315 (2022), 121523.
- [11] S. Qiu, W. Tang, S. Yang, J. Xie, D. Yu, O. Garcia-Rodriguez, J. Qu, S. Bai, F. Deng, A microbubble-assisted rotary tubular titanium cathode for boosting Fenton's reagents in the electro-Fenton process, *J. Hazard. Mater.* 424 (2022), 127403.
- [12] S.O. Ganiyu, M. Zhou, C.A. Martínez-Huitle, Heterogeneous electro-Fenton and photoelectro-Fenton processes: a critical review of fundamental principles and application for water/wastewater treatment, *Appl. Catal. B: Environ.* 235 (2018) 103–129.
- [13] S.O. Ganiyu, M.J.G. de Araújo, E.C. de Araujo Costa, J.E.L. Santos, E.V. dos Santos, C.A. Martínez-Huitle, S.B.C. Pergher, Design of highly efficient porous carbon foam cathode for electro-Fenton degradation of antimicrobial sulfanilamide, *Appl. Catal. B: Environ.* 283 (2021), 119652.
- [14] B. Jiang, Q. Niu, C. Li, N. Oturan, M.A. Oturan, Outstanding performance of electro-Fenton process for efficient decontamination of Cr (III) complexes via alkaline precipitation with no accumulation of Cr (VI): Important roles of iron species, *Appl. Catal. B: Environ.* 272 (2020), 119002.
- [15] H. Qi, W. Ren, X. Shi, Z. Sun, Hydrothermally modified graphite felt as the electro-Fenton cathode for effective degradation of diuron: The acceleration of Fe<sup>2+</sup> regeneration and H<sub>2</sub>O<sub>2</sub> production, *Sep. Purif. Technol.* 299 (2022), 121724.
- [16] J. Zhang, S. Qiu, H. Feng, T. Hu, Y. Wu, T. Luo, W. Tang, D. Wang, Efficient degradation of tetracycline using core-shell Fe@ Fe<sub>2</sub>O<sub>3</sub>-CeO<sub>2</sub> composite as novel heterogeneous electro-Fenton catalyst, *Chem. Eng. J.* 428 (2022), 131403.
- [17] Z. Ye, J.A. Padilla, E. Xuriguera, E. Brillas, I. Sirés, Magnetic MIL (Fe)-type MOF-derived N-doped nano-ZVI@C rods as heterogeneous catalyst for the electro-Fenton degradation of gemfibrozil in a complex aqueous matrix, *Appl. Catal. B: Environ.* 266 (2020), 118604.
- [18] S.B. Hammouda, C. Salazar, F. Zhao, D.L. Ramasamy, E. Lakova, S. Iftikhar, I. Babu, M. Sillanpää, Efficient heterogeneous electro-Fenton incineration of a contaminant of emergent concern-cotinine-in aqueous medium using the magnetic double perovskite oxide Sr<sub>2</sub>FeCuO<sub>6</sub> as a highly stable catalyst: Degradation kinetics and oxidation products, *Appl. Catal. B: Environ.* 240 (2019) 201–214.
- [19] S. Rezgui, A. Amrane, F. Fourcade, A. Assadi, L. Monser, N. Adhoum, Electro-Fenton catalyzed with magnetic chitosan beads for the removal of Chlordimeform insecticide, *Appl. Catal. B: Environ.* 226 (2018) 346–359.
- [20] Y. Li, C. Wang, S. Pan, X. Zhao, N. Liu, Mn doping improves in-situ H<sub>2</sub>O<sub>2</sub> generation and activation in electro-Fenton process by Fe/Mn@CC cathode using high-temperature shock technique, *Chemosphere* 307 (2022), 136074.
- [21] X. Li, C. Xiao, X. Ruan, Y. Hu, C. Zhang, J. Cheng, Y. Chen, Enrofloxacin degradation in a heterogeneous electro-Fenton system using a tri-metal-carbon nanofibers composite cathode, *Chem. Eng. J.* 427 (2022), 130927.
- [22] S. Cheng, C. Shen, H. Zheng, F. Liu, A. Li, OCNTs encapsulating Fe-Co PBA as efficient chainmail-like electrocatalyst for enhanced heterogeneous electro-Fenton reaction, *Appl. Catal. B: Environ.* 269 (2020), 118785.
- [23] W. Yang, M. Zhou, N. Oturan, M. Bechelany, M. Cretin, M.A. Oturan, Highly efficient and stable FeII/FeIII LDH carbon felt cathode for removal of pharmaceutical ofloxacin at neutral pH, *J. Hazard. Mater.* 393 (2020), 122513.
- [24] M. El Kateb, C. Trellu, A. Darwich, M. Rivallin, M. Bechelany, S. Nagarajan, S. Lacour, N. Bellakhal, G. Lesage, M. Heran, Electrochemical advanced oxidation processes using novel electrode materials for mineralization and biodegradability enhancement of nanofiltration concentrate of landfill leachates, *Water Res.* 162 (2019) 446–455.
- [25] H. Xu, H. Guo, C. Chai, N. Li, X. Lin, W. Xu, Anodized graphite felt as an efficient cathode for in-situ hydrogen peroxide production and Electro-Fenton degradation of rhodamine B, *Chemosphere* 286 (2022), 131936.
- [26] Y. Zhao, S. Hojabri, S. Sarrouf, A.N. Alshawabkeh, Electrogeneration of H<sub>2</sub>O<sub>2</sub> by graphite felt double coated with polytetrafluoroethylene and polydimethylsiloxane, *J. Environ. Chem. Eng.* 10 (2022), 108024.
- [27] Y. Gao, W. Zhu, Y. Li, Q. Zhang, H. Chen, J. Zhang, T. Huang, Anthraquinone (AQ)/polyaniline (PANI) modified carbon felt (CF) cathode for selective H<sub>2</sub>O<sub>2</sub> generation and efficient pollutant removal in electro-Fenton, *J. Environ. Manag.* 304 (2022), 114315.
- [28] C. Sun, T. Chen, Q. Huang, X. Duan, M. Zhan, L. Ji, X. Li, S. Wang, J. Yan, Biochar cathode: reinforcing electro-Fenton pathway against four-electron reduction by controlled carbonization and surface chemistry, *Sci. Total Environ.* 754 (2021), 142136.
- [29] M. Li, X. Qin, M. Gao, T. Li, Y. Lv, Graphitic carbon nitride and carbon nanotubes modified active carbon fiber cathode with enhanced H<sub>2</sub>O<sub>2</sub> production and recycle of Fe<sup>3+</sup>/Fe<sup>2+</sup> for electro-Fenton treatment of landfill leachate concentrate, *Environ. Sci.: Nano* 9 (2022) 632–652.
- [30] B.O. Orimolade, B.N. Zwane, B.A. Koiki, M. Rivallin, M. Bechelany, N. Mabuba, G. Lesage, M. Cretin, O.A. Arotiba, Coupling cathodic electro-fenton with anodic photo-electrochemical oxidation: a feasibility study on the mineralization of paracetamol, *J. Environ. Chem. Eng.* 8 (2020), 104394.
- [31] M.R. Haider, W.-L. Jiang, J.-L. Han, H.M.A. Sharif, Y.-C. Ding, H.-Y. Cheng, A.-J. Wang, In-situ electrode fabrication from polyaniline derived N-doped carbon nanofibers for metal-free electro-Fenton degradation of organic contaminants, *Appl. Catal. B: Environ.* 256 (2019), 117774.
- [32] H. Qi, X. Sun, Z. Sun, Porous graphite felt electrode with catalytic defects for enhanced degradation of pollutants by electro-Fenton process, *Chem. Eng. J.* 403 (2021), 126270.
- [33] H. Luo, X. Zhang, C. Xu, W. He, Z. Wang, W. Cai, Y. Zhang, Constructing a yolk-shell structure SiO<sub>2</sub>/C@C composite for long-life lithium-ion batteries, *ACS Appl. Energy Mater.* 5 (2022) 8982–8989.
- [34] C. Dong, S. Wang, M. Ma, P. Wei, Y. Chen, A. Wu, Z. Zha, H. Bi, Inhibition of oxidative stress in vivo through enzyme-like activity of carbon dots, *Appl. Mater. Today* 25 (2021), 101178.
- [35] F. Liu, Y. Zhang, S. Wang, T. Gong, M. Hua, J. Qian, B. Pan, Metal-free biomass with abundant carbonyl groups as efficient catalyst for the activation of peroxymonosulfate and degradation of sulfamethoxazole, *Chem. Eng. J.* 430 (2022), 132767.
- [36] G. Zhao, H. Zhao, L. Shi, B. Cheng, X. Xu, X. Zhuang, In situ loading MnO<sub>2</sub> onto 3D Aramid nanofiber aerogel as high-performance lead adsorbent, *J. Colloid Interface Sci.* 600 (2021) 403–411.
- [37] G. Wang, S. Zhang, J. Cui, W. Gao, X. Rong, Y. Lu, C. Gao, Preparation of nitrogen-doped carbon quantum dots from chelating agent and used as fluorescent probes for accurate detection of ClO<sup>-</sup> and Cr (VI), *Anal. Chim. Acta* 1195 (2022), 339478.
- [38] X. Zhang, M. Huangfu, J. Deng, Y. Wang, B. Wu, M. Hu, H. Zhao, S. Wu, Surface characteristics and flotation behaviours of specularite as influenced by lead ion modification, *Sep. Purif. Technol.* 276 (2021), 119384.
- [39] R.C. Rajak, P. Saha, M. Singhvi, D. Kwak, D. Kim, H. Lee, A.R. Deshmukh, Y. Bu, B. S. Kim, An eco-friendly biomass pretreatment strategy utilizing reusable enzyme mimicking nanoparticles for lignin depolymerization and biofuel production, *Green. Chem.* 23 (2021) 5584–5599.
- [40] K. Lakshmanan, W.H. Huang, S.A. Chala, B.W. Taklu, E.A. Moges, J.F. Lee, P. Y. Huang, Y.C. Lee, M.C. Tsai, W.N. Su, Highly active oxygen coordinated



- configuration of Fe single-atom catalyst toward electrochemical reduction of CO<sub>2</sub> into multi-carbon products, *Adv. Funct. Mater.* 32 (2022) 2109310.
- [41] K. Huan, Y. Li, D. Deng, H. Wang, D. Wang, M. Li, L. Luo, Composite-controlled electrospinning of CuSn bimetallic nanoparticles/carbon nanofibers for electrochemical glucose sensor, *Appl. Surf. Sci.* 573 (2022), 151528.
- [42] Y. Liu, Q. Xu, R. Guo, C. Duan, G. Wu, Y. Miao, J. Gu, Enhancement of the activity of Cu/TiO<sub>2</sub> catalyst by Eu modification for selective catalytic reduction of NOx with NH<sub>3</sub>, *Environ. Sci. Pollut. Res.* 27 (2020) 27663–27673.
- [43] F. Ansari, S. Sheibani, M. Fernandez-García, Surface modification of Cu<sub>2</sub>O-CuO photocatalyst on Cu wire through decorating with TiO<sub>2</sub> nanoparticles for enhanced visible light photocatalytic activity, *J. Alloy. Compd.* 919 (2022), 165864.
- [44] X. Huang, H. Li, Y. Zhang, R. Wu, L. Ban, L. Xi, Z. Yin, J. Peng, Y. Zhao, L. Fang, Enhancement of Cu<sup>+</sup> stability under a reducing atmosphere by long-range electromagnetic effect of Au, *Nanoscale* 14 (2022) 13248–13260.
- [45] R. Ranguin, M. Delannoy, C. Yacou, C. Jean-Marius, C. Feidt, G. Rychen, S. Gaspard, Biochar and activated carbons preparation from invasive algae *Sargassum* spp. for chlordecone availability reduction in contaminated soils, *J. Environ. Chem. Eng.* 9 (2021), 105280.
- [46] M. Xiang, Z. Lu, S. Li, H. Li, C. Wang, J. Zhang, L. Jin, C. Li, Magnetic core-shell S-Fe@MOF derivative hybrids to activate peroxymonosulfate for highly efficient degradation of tetrabromobisphenol A, *Sep. Purif. Technol.* 286 (2022), 120503.
- [47] Y. Zhao, B. Liang, X. Wei, K. Li, C. Lv, Y. Zhao, A core-shell heterostructured CuFe@NiFe Prussian blue analogue as a novel electrode material for high-capacity and stable capacitive deionization, *J. Mater. Chem. A* 7 (2019) 10464–10474.
- [48] A. Bhogi, P. Kistaiah, Thermal and structural characterization of lithium borate glasses doped with Fe (III) ions: The role of alkaline earths, *Opt. Mater.* 109 (2020), 110345.
- [49] I. Prakash, P. Muralidharan, N. Nallamuthu, M. Venkateswarlu, N. Satyanarayana, Simple and effective way to prepare CuFe<sub>2</sub>O<sub>4</sub>/SiO<sub>2</sub> nanocomposites by Sol-Gel method, *NSTI Nanotechnol. Conf. Trade Show 2* (2005) 4.
- [50] R. Shahbazi, M. Babazadeh, E. Afzali, Surface modification of silica-coated on the magnetic nanoparticles with covalently immobilized between imidazolium cation and silane groups for potential application as a green catalyst, *MOJ Bioorgan. Org. Chem.* 2 (2018) 11–17.
- [51] V.T. Huong, N.T.T. Phuong, N.T. Tai, N.T. An, V.D. Lam, D.H. Manh, T.T.K. Chi, N. X.D. Mai, V.-D. Phung, N.H.T. Tran, Gold nanoparticles modified a multimode clad-free fiber for ultrasensitive detection of bovine serum albumin, *J. Nanomater.* 2021 (2021) 1–6.
- [52] Y.M. de Matos, D.L. Vasconcelos, A.C. Barreto, J.E. Rocha, J.B. de Araújo-Neto, F. F. Campina, M.M.C. da Silva, T.T. Al Yafawi, C.E. Sobral-Souza, J.C. Pinheiro, Protection against the phytotoxic effect of mercury chloride by catechin and quercetin, *J. Chem.* 2022 (2022) 3770935.
- [53] T.X.H. Le, M. Bechelany, S. Lacour, N. Oturan, M.A. Oturan, M. Cretin, High removal efficiency of dye pollutants by electron-Fenton process using a graphene based cathode, *Carbon* 94 (2015) 1003–1011.
- [54] H.H.P. Quang, T.P. Nguyen, D.D.D. Nguyen, L.T.N. Bao, D. Nguyen, V.-H. Nguyen, Advanced electro-Fenton degradation of a mixture of pharmaceutical and steel industrial wastewater by pallet-activated-carbon using three-dimensional electrode reactor, *Chemosphere* 297 (2022), 134074.
- [55] Y. Liu, D. Zou, Y. Gao, Performance of high temperature phase-stable high entropy oxide (MgCuMnCoFe)O<sub>x</sub> in catalytic wet air oxidation of chloroquine phosphate, *J. Mater. Sci.* 57 (2022) 9104–9117.
- [56] M. Xu, J. Wei, X. Chen, G. Pan, J. Li, L. Xing, Y. Zhang, Y. Li, Z. Wang, J. Li, Satisfactory degradation of tetracycline by a pH-universal MnFe-LDH@BC cathode in electric Fenton process: performances, mechanisms and toxicity assessments, *J. Environ. Chem. Eng.* 10 (2022), 108409.
- [57] J. Wang, J. Qin, B. Liu, S. Song, Reaction mechanisms and toxicity evolution of sulfamethoxazole degradation by CoFe-N doped C as Electro-Fenton cathode, *Sep. Purif. Technol.* 298 (2022), 121655.
- [58] P. Cao, X. Quan, K. Zhao, S. Chen, H. Yu, J. Niu, Selective electrochemical H<sub>2</sub>O<sub>2</sub> generation and activation on a bifunctional catalyst for heterogeneous electro-Fenton catalysis, *J. Hazard. Mater.* 382 (2020), 121102.
- [59] S. Qiu, Y. Wang, J. Wan, Y. Ma, Z. Yan, S. Yang, Enhanced electro-Fenton catalytic performance with in-situ grown Ce/Fe@NPC-GF as self-standing cathode: fabrication, influence factors and mechanism, *Chemosphere* 273 (2021), 130269.
- [60] M. Mohseni, W. Zängler, K. Demeestere, G. Du Laing, S. Bhandari, A.K. Mechler, S. Yüce, R.G. Keller, M. Wessling, One-pot synthesized, Fe-incorporated self-standing carbons with a hierarchical porosity remove carbamazepine and sulfamethoxazole through heterogeneous electro-Fenton, *Chem. Eng. J.* 446 (2022), 137006.
- [61] Y. Wang, H. Zhang, B. Li, M. Yu, R. Zhao, X. Xu, L. Cai, γ-FeOOH graphene polyacrylamide carbonized aerogel as air-cathode in electro-Fenton process for enhanced degradation of sulfamethoxazole, *Chem. Eng. J.* 359 (2019) 914–923.
- [62] H. Qi, X. Sun, Z. Sun, Cu-doped Fe<sub>2</sub>O<sub>3</sub> nanoparticles/etched graphite felt as bifunctional cathode for efficient degradation of sulfamethoxazole in the heterogeneous electro-Fenton process, *Chem. Eng. J.* 427 (2022), 131695.
- [63] Y. Li, Y. Yang, J. Lei, W. Liu, M. Tong, J. Liang, The degradation pathways of carbamazepine in advanced oxidation process: a mini review coupled with DFT calculation, *Sci. Total Environ.* 779 (2021), 146498.
- [64] J. Guo, H. Sun, X. Yuan, L. Jiang, Z. Wu, H. Yu, N. Tang, M. Yu, M. Yan, J. Liang, Photocatalytic degradation of persistent organic pollutants by Co-Cl bond reinforced CoAl-LDH/Bi<sub>12</sub>O<sub>17</sub>Cl<sub>2</sub> photocatalyst: mechanism and application prospect evaluation, *Water Res.* 219 (2022), 118558.